OPEN-CHANNEL TURBULENT FLOW OVER TWO DIMENSIONAL SQUARE RIBS

A Thesis
Submitted to the Faculty of Graduate Studies
In Partial Fulfillment of the Requirements for the Degree of

Master of Science

in the

Department of Mechanical and Manufacturing Engineering
University of Manitoba
Winnipeg, Manitoba
Canada

By

SHASHIDHAR MAKKAPATI
July, 2006

THE UNIVERSITY OF MANITOBA

FACULTY OF GRADUATE STUDIES

*****

COPYRIGHT PERMISSION

OPEN-CHANNEL TURBULENT FLOW OVER TWO DIMENSIONAL SQUARE RIBS

BY

SHASHIDHAR MAKKAPATI

A Thesis/Practicum submitted to the Faculty of Graduate Studies of The University of Manitoba in partial fulfillment of the requirement of the degree

OF

MASTER OF SCIENCE

ABSTRACT

This thesis presents an experimental investigation of open-channel turbulent flow over two-dimensional transverse ribs. The ribs comprise square rods placed on the channel floor at regular pitch. The side of the square rods was kept constant but the pitch between adjacent rods was varied to produce the so-called *d*-type, intermediate, and *k*-type roughness. Two depths of water column, $h = 45$ mm and $h = 35$ mm were investigated. A particle image velocimetry (PIV) was used to conduct detailed velocity measurement on a smooth-wall and over the three rib types. The Reynolds number based on the rib height and approach freestream velocity was $Re_k \approx 1550$. The ratios of rib height to depth of water columns were 0.13 and 0.17. From the PIV measurements, the mean velocity, turbulent intensities, Reynolds shear stress, streamlines and contours of vorticity were obtained to study the effects of pitch-to-height ratio on the flow characteristics. The results show that the cavities between the *d*-type and intermediate ribs are completely occupied by stable vortices which prevent the outer flow from reattaching onto the cavity floor. On the other hand, the outer flow reattached onto the floor of the *k*-type cavities. As a result, the flow above the *k*-type ribs is significantly inhomogeneous. The results also show that the drag and turbulence levels increase substantially with increasing pitch-to-height ratio. The similarities and differences between the present study and previous studies over two-dimensional square ribs in turbulent boundary layers and fully developed channels are documented.

ACKNOWLEDGEMENTS

I would like to express my sincere appreciation and gratitude to my supervisor, Dr. Mark Francis Tachie for giving me the opportunity to work in this challenging field of research. His invaluable help with all aspects of this thesis as well as with my graduate course work is greatly appreciated.

I am also grateful to my colleagues Mr. Mohammad Khalid Shah, Mr. Martin Agelinchaab and Mr. Samuel Sunday Paul for their co-operation during the course of experimentation. My appreciation also goes to Mr. Kofi Adane for his assistance during the development of Matlab code.

In conclusion, I would like to take this occasion to express my sincere thankfulness to my parents Mr. and Mrs. Durga Prasad Sarma, and my brother Muralidhar Makkapati, for their love and invaluable input into my education over the years.

DEDICATION

This thesis is dedicated to my parents, Durga Prasad Sarma and Saraswathi Devi, for giving me the necessary support to pursue my studies.

TABLE OF CONTENTS

LIST OF TABLES

LIST OF FIGURES

NOMENCLATURE

English Symbols

B, C	Log-law constants
B	Bias component of uncertainty
C_d	Seeding density
C_f	Skin friction coefficient
C_p	Pressure coefficient
d_I	Seeding particle image diameter
d_p	Seeding particle diameter
dx, dy	Distance moved by the seeding particle in x and y directions
dP/dx	Pressure gradient
$\partial V/\partial x$	Wall-normal velocity gradient
$\partial U/\partial y$	Streamwise velocity gradient
Δt	Elementary bias in the time between two laser pulses
E	Total uncertainty
Fr	Froude's number
$f_{\#}$	f-number of the CCD camera lens
g	Acceleration due to gravity
h	Depth of water column
k	Rib height
k_s	Sand grain roughness
k_s^+	Roughness Reynolds number

K	Confidence coefficient
L_0	Field of view of the CCD camera
L_I	Interrogation area size
M	Image magnification
N	Number of readings
N_I	Seeding particle image density
p	Pitch or distance between crests of adjacent ribs
P	Precision component of measurement uncertainty
P_d	Pressure drag
Re_h	Reynolds number based on freestream velocity and depth of the water
Re_θ	Reynolds number based on freestream velocity and momentum thickness
Re_τ	Reynolds number based on friction velocity and depth of water
Re_k	Reynolds number based on freestream velocity and rib height
Re_p	Reynolds number of the seeding particles
Δs	Elementary bias in CCD pixel
S	Scale factor
t	time
T	Mean temperature
ΔT	Minimum time interval between images
U	Streamwise component of mean velocity
V	Wall-normal component of mean velocity
U_e	Freestream velocity

U_{min}	Minimum velocity
U_τ	Friction velocity
u, v, w	Fluctuating velocity components in streamwise and wall-normal directions
u, v	Co-ordinates of spatial frequency domain
$-<uv>$	Reynolds shear stress
v_s	Settling velocity of seeding particles
Δz	Light sheet thickness
x'	axial location corresponding to rib-top
x, y, z	Streamwise, wall-normal and spanwise co-ordinates

Greek Symbols

β	Clauser equilibrium parameter
δ	Boundary layer thickness
δ^*	Displacement thickness
λ	Solidity of ribs, wave length of the laser light
κ	Von Karman constant
Ω_z	Mean spanwise vorticity
μ	Dynamic viscosity
Π	Coles wake parameter
υ	Kinematic viscosity
ρ	Density
ρ_p	Density of the seeding particles
ρ_f	Density of the fluid

ρ_{uu}, ρ_{vv}	Two point correlation coefficients
τ_R	Response time of the seeding particles
τ_w	Wall shear stress
θ	Boundary layer momentum thickness
θ_X	Sensitivity coefficient for variable X
σ	Standard deviation
ΔU^+	Roughness shift

Sub scripts and super scripts

$()^+$	Normalization in wall units U_τ and v/U_τ
$()_X$	Bias limit, precision limit, sensitivity coefficients at variable X
$()_{max}$	Peak value of any quantity

Functions

f(m, n)	Light intensity function at time t
g(m, n)	Light intensity function at time $t + \Delta t$
d(m, n)	Noise function
s(m, n)	Transfer function
F(u, v)	Fourier transformations of f(m, n)
G(u, v)	Fourier transformations of g(m, n)
D(u, v)	Fourier transformations of d(m, n)
S(u, v)	Fourier transformations of s(m, n)
Φ(u, v)	Cross-correlation function

Abbreviations

CCD	Charged coupled device
DNS	Direct numerical simulation
FFT	Fast Fourier transformations
FFT^{-1}	Inverse Fast Fourier transformations
LDA	Laser Doppler anemometry
LDV	Laser Doppler velocimetry
LES	Large eddy simulation
LIF	Laser induced florescence
PIV	Particle image velocimetry
T.K.E	Turbulent kinetic energy

CHAPTER 1

INTRODUCTION

1.1 Background

Open-channel flows are a special case of boundary layer flows. These flows are important from the standpoint of environmental fluid mechanics as many of the naturally occurring flows are open-channel in nature. Examples include flows in rivers and oceans, flow of sewage wastes, and in some industrial applications. The study of turbulence characteristics of open-channel flows also finds numerous applications in marine and hydraulic engineering. Turbulent flows over rough surfaces have considerable engineering interest due to the increased transport of heat, mass and momentum (Krogstad and Antonia, 1999). The phenomenon such as turbulent transport, diffusion and resistance are connected with distribution of mean velocity, turbulent intensity and other statistical characteristics of the turbulent structure.

Despite its numerous applications, physical understanding of turbulent flows over rough surfaces is incomplete. The roughness makes the analysis of these flows complex as the roughness scales usually vary from regular two-dimensional roughnesses to an irregular three-dimensional manufacturing roughness. For a rough surface, the wall boundary conditions become more complex than a smooth surface because the flow is no longer parallel to the ground plane. Instead, the details of the flow in the roughness sublayer depend on the specific geometry of the roughness elements (Bergstrom et al., 2002). In many cases, the roughness elements resemble bluff body structures attached to a ground plane and the flow structure is dominated by the bluff body wakes formed by the roughness elements.

Nikuradse (1933) was one of the first researchers to study turbulent flow through fully developed pipes roughened by sand grains. His results show that the most obvious effect of roughness is the change in the mean velocity profile near the wall and a consequent modification of the friction coefficient. Nikuradse (1933) suggested that for rough-wall turbulent flows, the classical log-law which is used for smooth surfaces can be used with minor modifications. Raupach et al. (1999) predicted that wall roughness effects are likely pronounced in the roughness sublayer which is defined as the inner layer up to a distance of about 4 to 5 roughness heights. In the roughness sublayer, the roughness elements will strongly interact with the streamwise vortices found near the walls, so that the inner region is expected to be severely modified compared to a smooth-wall flow. In the outer layer, however, the flow is expected to be unaffected by the mechanism that produces the turbulence in the inner layer and therefore should behave very similar to the smooth-wall flows.

1.2 Roughness classification

It is a common knowledge that, in the limit of infinite Reynolds number, every surface will tend to behave as rough. In nature, there exist infinite number of surfaces and geometries, for example, pebbles, sand grains, wire-mesh and transverse ribs can create roughness. Irrespective of the way the roughness is created, it can be classified into two broad categories, *k*-type and *d*-type, based on its effect on the flow field.

1.2.1 *k* – type roughness

According to Jimenez (2004), if the value of $k_s^+ >> 1$ (roughness Reynolds number much greater than unity), the viscosity of the fluid becomes irrelevant and k_s (equivalent sand roughness) would be proportional to the dimensions of the roughness elements. The surfaces which satisfy the above criterion are usually termed as *k*-type roughness. For these surfaces the ratio k_s/k depends on the solidity of the roughness elements. The solidity λ can be defined as the total projected frontal roughness area per unit wall-parallel projected area. Schlichting (1936) found a quantitative relation between the solidity of the roughness elements and ratio between k_s and k. Most of the quantitative correlations are available only for regular geometries which can be easily described. As stated by Jimenez (2004), walls with grooves wider than $3 \sim 4\ k$ will have a recirculation bubble that reattach well ahead of the next rib, exposing the roughness effects into the outer flow as shown in figure 1.1(a). Tani (1987) suggested that, in case of ribs arranged at regular pitch, *k*-type roughness is typified by sparsely spaced transverse ribs with a pitch ratio p/k greater than 4, where p is the pitch between two adjacent ribs. This type of roughness generates eddies of length scale of the order of roughness elements height and penetrate towards the channel or pipe center. The roughness function and friction factor values depend on the size of the roughness elements.

1.2.2 *d* – type roughness

Perry et al. (1969) were one of the earlier researchers who have summarized the *d*-type roughness behavior. They pointed out that, for *d*-type rough surfaces effective roughness k_s was not proportional to the roughness height k, but to the boundary layer thickness δ.

Although the results are true for zero pressure gradient boundary layers, this may not be applicable for other cases. Jimenez (2004) suggested that the grooves of *d*-type walls are roughly square, with a solidity of $\lambda = 0.5$ and they sustain stable recirculation vortices that isolate the outer flow from the roughness. However, Tani (1987) suggested that for regularly arranged ribs, the *d*-type roughness is characterized by a pitch ratio of $p/k < 4$. He also suggested that the roughness function in this case is independent of the size of the roughness elements and the ribs are so closely spaced that the stable vortices are set up in the grooves. As shown in figure 1.1(b), the eddy shedding from the roughness elements into the outer flow is negligible.

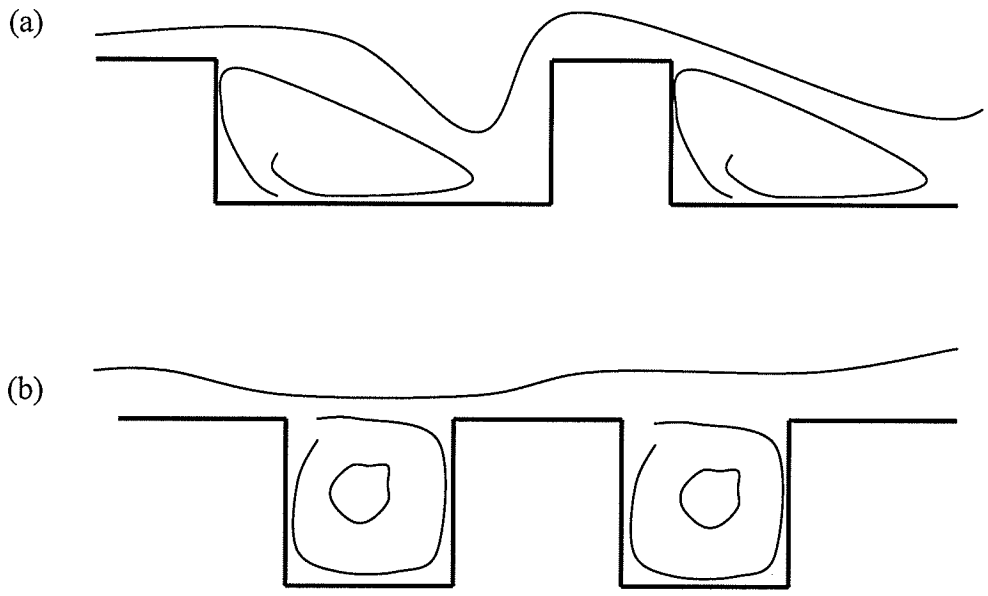

Fig. 1.1 Geometry of (a) *k*-type roughness (b) *d*-type roughness in slotted-wall flows

1.3 Motivation

The present work has drawn motivation from the numerical studies of Cui et al. (2003) and experimental results of Okamoto et al. (1993). Rib pitch-to-height ratios were selected based on the criterion explained in the LES studies of Cui et al. (2003) for the creation of *k*-type, intermediate and *d*-type roughness. Although there exists numerous numerical and limited experimental literature related to the rib-roughened channel flows, most of the analysis are related to heat transfer applications. To the best of author's knowledge there has not been detailed analysis of mean velocities and turbulent quantities over transverse ribs in open-channel flows. It is therefore believed that employing high resolution PIV to make detailed velocity measurements for different pitch-to-height ratios will provide better insight into the turbulent flow phenomenon.

CHAPTER 2

LITERATURE REVIEW

2.1 Introduction

This chapter outlines the scaling laws for near-wall turbulent flows and summarizes the previous literature on turbulent flows over rough surfaces. The previous literature is divided into two parts namely experimental studies and numerical studies. The experimental studies are sub-divided into random three-dimensional roughness elements and two-dimensional transverse ribs or roughness elements. The specific objectives of the present work are also stated at the end of the chapter.

2.2 Scaling Consideration

2.2.1 Turbulent flow over smooth-wall

The two-layer concept forms the basis of analyzing near-wall turbulent flows. The flow is divided into inner and outer layers. In the inner layer, the mean velocity, U, at any distance from the wall is assumed to depend on the distance from the wall, y, the wall shear stress, τ_w, fluid density, ρ, and dynamic viscosity, μ. The mean velocity is expressed in the following non-dimensional form:

$$U^+ = f(y^+) \qquad [2.1]$$

where $U^+ = U/U_\tau$, $y^+ = yU_\tau/\nu$, ν is the kinematic viscosity, and $U_\tau = (\tau_w/\rho)^{1/2}$ is the friction velocity. Equation [2.1] is often referred to as the universal law of the wall. Hereafter, superscript "+" will be used to denote normalization in wall units, that is, U_τ and ν/U_τ. In the outer layer, the wall acts to retard the local velocity, U, below the freestream velocity,

U_e, in a manner that is independent of viscosity, but dependent on the distance from the wall, y, the boundary layer thickness, δ, the wall shear stress, τ_w, and freestream pressure gradient, dP/dx. The mean velocity for this region is presented in a non-dimensional form as follows:

$$U_e^+ - U^+ = g(y/\delta, \beta) \qquad [2.2]$$

where $\beta = (\delta^*/\tau_w)\, dP/dx$ is the Cluaser equilibrium parameter, and $\delta^* = \int_0^\infty \left(1 - \frac{U}{U_e}\right) dy$ is the displacement thickness. Equation [2.2] is called the velocity defect law.

At a sufficiently high Reynolds number, an overlap region exists between the inner and outer layers where both layers interact. Millikan (1938) matched Equation [2.1] and [2.2] to obtain the following log-laws for the overlap region:

$$U^+ = \kappa^{-1} \ln(y^+) + B \qquad [2.3]$$

$$U_e^+ - U^+ = \kappa^{-1} \ln(y/\delta) + B \qquad [2.4]$$

where the von Karman constant, κ and B are assumed to be universal and independent of Reynolds number. In this thesis, the following values are adopted: $\kappa = 0.41$ and $B = 5.0$. Coles (1956) added a wake function to the log-law to describe both the overlap and outer regions of the boundary layer:

$$U^+ = \kappa^{-1} \ln(y^+) + B + 2\Pi/\kappa\, w(y/\delta) \qquad [2.5]$$

where Π is Coles wake parameter and w is a universal function of y/δ.

2.2.2 Turbulent flow over rough surfaces

When the surface is rough, the characteristic length scales may also include the average roughness height, k and any additional length scales needed to completely characterize the roughness. It is often assumed that roughness effects on the turbulence structure are confined to the immediate vicinity of the roughness elements. This region is referred to as the roughness sublayer and is defined as the distance extending from the wall up to 5 roughness heights (Raupach et al., 1991). Outside the roughness sublayer, turbulent motions are considered to be independent of the wall roughness at sufficiently high Reynolds number. Following Clauser (1954) and Hama (1954), the mean velocity profiles in the overlap region, and both the overlap and outer regions are, respectively, expressed as:

$$U^+ = \kappa^{-1} \ln(y^+) + B - \Delta U^+ \qquad [2.6]$$

$$U^+ = \kappa^{-1} \ln(y^+) + B - \Delta U^+ + 2\Pi/\kappa\, w(y/\delta) \qquad [2.7]$$

where ΔU^+ is the roughness function which represents the (parallel) downward shift between smooth-wall and rough-wall velocity profiles on a Clauser plot. The specific value of ΔU^+ depends on the roughness Reynolds number, $k_s^+ = k_s U_\tau/\nu$, as well as the roughness geometry. The sand grain roughness Reynolds number $k_s^+ = k_s U_\tau/\nu$ based on equivalent sand roughness height k_s is related to the roughness function as follows (Ligrani and Moffat, 1986):

$$\Delta U^+ = \kappa^{-1} \ln(k_s^+) + B - C \qquad [2.8]$$

where $C = 8.5$. Schlichting (1979) proposed the following three roughness classifications: hydraulically smooth ($k_s^+ < 5$), transitionally rough ($5 \leq k_s^+ \leq 70$) and fully rough $k_s^+ > 70$.

2.2.3 Open-channel flows

As previously mentioned in Chapter 1, open-channel flows are a special case of boundary layer flows, so the analysis of open-channel flows is approximately similar to boundary layer flows. The log-law constants used in these analyses are the same as those used in boundary layer flows.

2.3 Review of previous studies

2.3.1 Measurements over three-dimensional roughness elements

Because of their technological importance, turbulent flows over rough surfaces have been studied quite extensively following the sand roughness studies by Nikuradse (1933). Different roughness elements such as sand grains, gravels, spheres, wire mesh, and two-dimensional ribs attached to surfaces have been used in the past to model surface roughness. Hama (1954), Acharya et al. (1985), Antonia et al. (2000), Balachandar et al. (2004), Akinlade et al. (2004), Bergstrom et al. (2005) examined turbulent flows over sand beds, wire mesh and perforated surfaces. Sleath (1988) studied turbulent flow over rough beds containing sand and gravels in connection with the measurement of turbulent intensity in oscillatory flow in water tunnel.

2.3.2 Measurements over transverse ribs

Because it is impractical to review all prior measurements over two-dimensional ribs, only selected and representative works are summarized in Table 2.1. Liou and Kao (1988) conducted experimental studies on turbulent flows in rectangular ducts with a pair of ribs arranged on the top and bottom walls of the channel. The objectives of the study were to experimentally characterize the turbulent flow using Laser Doppler Velocimetry (LDV). The study was conducted for both symmetric and asymmetric patterns of ribs. The test matrix contained various rib heights and widths to determine their effects, on the reattachment length. The study included four pitch ratios in the range, $2 \leq p/k \leq 6.5$. The Reynolds number based on hydraulic diameter of the duct and bulk velocity of the flow varied between 2,000 and 76,000. The measurements were obtained at 23 locations which include upstream, downstream and around the rib configuration. Mean velocities and turbulent intensities for different cases were presented. It was reported that a critical rib height exists above which the flow patterns become asymmetric downstream of the rib leading corners. It was observed that the reattachment length behind the rib first decreases up to a pitch ratio of 5 and remain nearly constant thereafter. Furthermore, it was observed that boundary layer thickness also affects the reattachment length behind the ribs.

Sato et al. (1989) also conducted experimental study in a rectangular channel. Two-dimensional square ribs of 10 mm side were arranged on the top and bottom walls of the channel. Three different rib configurations were investigated namely symmetry, staggered and unsymmetry. A rib roughness ratio of 7 was maintained for all the rib configurations. The measurements were conducted using LDV and the Reynolds number

based on average velocity in the channel and distance between the ribbed walls was 20,000. The goal of the study was to compare the mean and turbulent intensities for the above mentioned rib configurations. The streamwise measuring location was the same for all the cases and was set at seven pitch (7 times the height of the rib) distance from the inlet of the test section. They reported that the rib configuration has no significant effect on static pressure distribution and shows only a modest effect on the mean velocity. However, the rib configuration has remarkable influence on the turbulent characteristics of the flow. It was also reported that the rib may influence the generation of turbulence energy and will also generate a strong correlation of velocity fluctuations. It was concluded from the results of the friction factor for three different rib configurations that unsymmetrical rib configuration will be more suitable for upgrading the performance of the heat transfer enhancement.

Mullin and Martin (1991) conducted experiments on intermittent phenomena in the flow over a rib-roughened surface in a two-dimensional water channel. Ribs of square cross-section of 5 mm side were arranged on the bottom wall of the channel. The principal objective of the study was to investigate the intermittent formation of a separation bubble near the leading edge of each rib. A pitch-to-height ratio of 7.2 was studied using LDV. The measurement location was fixed at rib number 29 from the inlet. The measurements included half of the front face of the rib and extending 0.9 mm into the freestream. It was reported that a small recirculation bubble was formed along the leading edge of each rib and subsequently collapses at irregular intervals. There was evidence of temporally correlated flow behavior centered on a frequency of 5 Hz which corresponds to a Strouhal number of 0.1.

Okamoto et al. (1993) conducted experimental study to investigate the effect of two-dimensional square ribs on the shear flow and heat transfer characteristics. Two-dimensional square ribs of side 10 mm were arranged on the ground plane of the channel at regular pitch. The goal of the study was to analyze the flow structure over repeated two-dimensional square ribs for various pitch-to-height ratios and to find the optimum pitch-to-height ratio that will augment turbulence. The experimental data were obtained for p/k = 2, 5 and 9. The mean velocities, static pressure and velocity vectors were measured using pitot and static pressure tubes and three hole cylindrical yawmeter. The turbulent intensities and integral length scales were measured using hot wire anemometry and temperatures were measured using thermocouples. It was reported that the pitch-to-height ratio of 9 was optimum to augment turbulence and heat transfer. Incase of pitch-to-height ratio of 9, the streamline leaving a rib corner was found to reattach to the ground plate at a distance of about four times the rib height. The turbulence intensity observed was largest immediately downstream of the reattachment point and decreased gradually to the next rib.

Islam et al. (2004) conducted experimental study to analyze the turbulent flow structure in a fully developed rib-roughened channel using particle image velocimetry (PIV). Square cross-sectioned ribs of side 4 mm were arranged on the top wall of the channel. The principal objective of the study was to investigate basic turbulent flow structure that occurs at upstream, center and downstream of the ribs for two different rib pitch-to-height ratios of 10 and 20. The Reynolds numbers based on freestream velocity and half channel height varied from 7,000 to 20,000. It was observed that rotating and counter rotating eddies were formed at the rib height. A relatively high level of

turbulence was observed just above the rib height for downstream location and relatively low level of turbulence was observed at twice the rib height. The reattachment length was found to be dependent on the Reynolds number up to a value of 15,000 and became independent beyond this value. The reattachment length observed was approximately four times the rib height. It was suggested that the higher rib pitch-to-height ratio (p/k = 20) contribute to higher level of turbulence up to a certain Reynolds number (Re_h = 20,000) compared to the smaller ratios (p/k = 10) investigated in their study. However, this may not be beneficial as it will result in higher pressure rise without major changes in reattachment length.

More recently, Krogstad et al. (2005) conducted experimental and numerical study of channel flow with rough-walls. The top and bottom walls of the channel were arranged with transverse square ribs of side 1.7 mm which is equal to nearly 3.4% of the half channel height. The study examined a pitch-to-height ratio of 8. The goal of the study was to compare the rib-roughened channel flow with corresponding data over a smooth surface using experimental (hot-wire anemometry) and numerical (direct numerical simulation, DNS) techniques.

2.3.3 Numerical studies

Some selected numerical works are summarized in Table 2.2. Meng et al. (1999) were one of the earlier researchers who used large eddy simulation (LES) with dynamic sub grid stress (SGS) model to study turbulent channel flow with rib-roughened wall. The roughness elements were arranged at regular distances on the channel floor. A blockage ratio (ratio of height of the roughness element to the height of the channel) of 0.2 was

maintained in the study. The study was mainly focused on the pitch ratio of 7.2 at Reynolds number based on the channel height and reference velocity of 20,000. To make use of periodic boundary conditions in the streamwise direction, the computational area was assumed to be embedded in a periodic array of many ribs in a fully developed flow. One of the goals of the study was to evaluate the merits of the dynamic SGS model for rib-roughened channel flow. It was reported that numerical results are in good agreement with prior experimental results. It was suggested that the increase in turbulence statistics and complex patterns observed upstream of the rib (used in the computational domain) is responsible for heat transfer enhancement for channel flow with a rib.

Cui et al. (2003) used LES with dynamic sub-grid-scale model to study turbulent flow in a rib-roughened channel. Two-dimensional square ribs of side equal to 10% of channel height were arranged at regular distances on the channel floor. The Reynolds number of the flow (based on the half channel height and bulk velocity of the flow) was maintained at 10,000. The goal of the study was to investigate the turbulence structure associated with *d*-type, intermediate and *k*-type roughness. The pitch-to-height ratios studied were $p/k = 2$, 5 and 10. The study presents the time averaged mean and turbulent intensity values and provides some new findings of the effect of the roughness on the mean and turbulent structure of the flow. It was also reported that the limit of the *d*-type roughness appears to be a pitch ratio of 5, where the eddy just fills the cavity and the reattachment occurs on the top of the downstream rib. It was also observed that beyond a pitch ratio of 5, the main eddy in the groove between the ribs is about four times the rib height long. There were also several small counter rotating eddies so that the rib can be termed as *k*-type.

Recently, Leonardi et al. (2003) conducted a DNS of fully developed turbulent channel flow with a smooth upper wall and transverse square ribs on the bottom wall. The goal of the study was to examine in detail how the skin friction drag and form drag depend on p/k, and also to estimate the roughness shift (ΔU^+) and its dependence on p/k. To achieve these goals, four simulations were performed by varying the rib height and Reynolds number of the flow. A combination of Reynolds number $Re_h = 4200$, $k = 0.2\ h$; $Re_h = 8400$, $k = 0.1\ h$, $0.15\ h$; $Re_h = 10400$, $k = 0.1\ h$ were tested for different pitch values between the ribs As a result of different pitch, they investigated pitch-to-height ratios in the range of $2 \leq p/k \leq 20$. They indicated that the results were not affected by the blockage caused by the ribs. The skin frictional drag C_f and the form drag P_d were determined for various values of the pitch-to-height ratios. It was observed that the minimum skin frictional drag and maximum pressure drag occur at a pitch-to-height ratio of 8. It was also mentioned that the roughness function (ΔU^+) variation with pitch-to-height ratio compares favorably with the prior experimental works.

In a subsequent paper, Leonardi et al. (2004) discussed how the rib pitch-to-height ratio influences the organized structures near the wall in channel flows with smooth upper wall and roughened bottom wall. They pointed out that, near a rough-wall, the turbulent structure is less elongated than over a smooth-wall. The changes observed in the turbulent structure may account for the strength of outward ejections of fluid from the cavities. They indicated that the strength observed is maximum for $p/k = 8$. They also reported that, for $p/k \leq 3$, the structures and turbulent intensities resemble those over a smooth-wall. For $p/k = 4$, effects of the wall extends up to about two times the height of the roughness element ($2k$) above the plane of the crests and incase of $p/k = 8$, the wall

effects are felt up to five times the height of the roughness element ($5k$) above the plane of the crests. For $p/k > 8$, the wall-normal motion induced by the roughness is confined to smaller regions, and the overlying flow is closer to that above a smooth-wall. They observed that the pitch ratio, $p/k = 8$, corresponds to that for which the roughness function ΔU^+ is largest.

Nagano et al. (2004) conducted DNS of velocity and thermal fields in turbulent channel flow with transverse rib-roughness on the bottom wall of the channel. A finite difference method was employed for analyzing the velocity and thermal fields by varying the spacing, height and width of the ribs in order to simulate the *k*-type and *d*-type roughness. The goal of the study was to obtain detailed knowledge of the effects of roughness elements on both the velocity and thermal fields in the near wall region, and to obtain the optimal rib arrangement to promote heat transfer as well as turbulence thermal structure from various view points. The study was conducted for four different pitch-to-height ratios ($p/k = 2$, 4, 8 and 16). It was observed that the skin friction coefficient and Nusselt number over the ribs are larger in comparison with those obtained over a smooth-wall.

Alireza et al. (2004) conducted a numerical investigation to study turbulent flow in a square rib-roughened channel. The top and bottom walls of the channel were roughened by square ribs of side k equal to 1.7% of the channel height. The principal objective of the study was to investigate the roughness effects on the mean and turbulent flow fields, and also to examine how far from the near-wall region these effects are felt. The relative height of the roughness elements considered for the study was considerably smaller than the prior studies. The study examined a pitch-to-height ratio of 8, which

corresponds to a k-type roughness. This pitch-to-height ratio was specifically chosen for the study to explore the configuration in which the roughness was known to have the largest influence on the mean flow field. The results presented show that the averaged streamline pattern exhibits two co-rotating vortices in the cavity between any two adjacent ribs. It was suggested that the fairly large extent of the roughness effects was due to the occasionally vigorous fluid motion originating from the cavities. The roughness shift value ΔU^+ in the mean velocity profile was 7, suggesting the flow field to be transitionally rough.

Author	Pitch ratio (*p/k*)	Reynolds number	Measurement technique	Quantities measured
Liou and Kao (1988)	2 - 6.5	$2{,}000 < Re_h < 76{,}000$	LDV	U, u ,v
Sato et al. (1989)	7	$Re_h = 20{,}000$	LDV	U, u, v, $-\langle uv \rangle$
Mullin and Martin (1991)	7.2	$Re_h = 21{,}250$	LDV	Power spectrum of U, V
Okamoto et al. (1993)	2 , 5, 9	$Re_k = 7{,}500$	Pitot and static pressure tube	U, u, T, P_s
Djenidi et al. (1999)	2	$900 < Re_\theta < 2300$	LDV / LIF	U, V, u, v, $-\langle uv \rangle$
Islam et al. (2004)	10, 20	$7000 < Re_h < 20{,}000$	PIV	U, T.K.E
Krogstad et al. (2005)	8	$Re_h = 6{,}000$	Hot wire anemometry	U, u, v, w, $-\langle uv \rangle$

Table 2.1 Summary of previous experiments over transverse ribs

LDV = Laser Doppler Velocimetry; PIV = Particle Image Velocimetry; LIF = Laser Induced Florescence; U, V = mean velocities; u, v, w = turbulent fluctuations; $-\langle uv \rangle$ = Reynolds shear stress; P_s = static pressure distribution; T.K.E = turbulent kinetic energy; Re_h = Reynolds number based on channel height and freestream velocity; Re_θ = Reynolds number based on momentum thickness and freestream velocity; Re_k = Reynolds number based on rib height and freestream velocity.

Author	Pitch ratio (*p/k*)	Blockage ratio (*k/h*)	Reynolds number	Numerical Technique	Quantities Reported
Meng et al. (1999)	7.20	0.20	$Re_h = 20{,}000$	LES	U, u, $-\langle uv \rangle$
Cui et al. (2003)	2, 5, 10	0.10	$Re_h = 10{,}000$	LES	U, u, v, $-\langle uv \rangle$, C_f, C_p
Leonardi et al. (2003)	2 - 20	0.10, 0.20	$Re_h = 4{,}200$-10,400	DNS	U, C_f, P_d
Leonardi et al. (2004)	2 - 20	0.10, 0.20	$Re_h = 4{,}200$	DNS	U, ρ_{uu}, ρ_{vv}
Nagano et al. (2004)	2, 4, 8,16	0.03, 0.05, 0.10	$Re_\tau = 150$	DNS	U, u, v, w, $-\langle uv \rangle$, T.K.E, C_f
Alireza et al. (2004)	8	0.02	$Re_\tau = 400$	DNS	U, u, v, $-\langle uv \rangle$, T.K.E , C_f

Table 2.2 Summary of previous numerical studies over transverse ribs

LES = Large eddy simulation; DNS = Direct numerical simulation; U = mean velocity; u, v = turbulent fluctuations; $-\langle uv \rangle$ = Reynolds shear stress; T.K.E = Turbulent kinetic energy; C_f = Skin friction coefficient; C_p = Pressure coefficient; P_d = pressure drag; ρ_{uu}, ρ_{vv} = Two point correlation coefficients.

2.4 Summary of literature review

In sections 2.3 and 2.4, a detailed review of literature on experimental and numerical studies was carried out. The literature suggests that a great deal of experimental and numerical research was conducted in rib-roughened channel flows. After reviewing the literature it is clear that a detailed analysis of open-channel turbulent flow over two-dimensional square ribs using PIV was not yet done.

2.5 Objectives of the study

In the present thesis experiments were conducted to measure the mean and turbulent quantities in a rib-roughened open-channel turbulent flow. To avoid contact of the instrumentation with the fluid, particle image velocimetry (PIV) technique was employed. The effect of the rib spacing on the mean and turbulent quantities was investigated for two different velocities in the study.

The goals of this research can be summarized as following

- To study the effect of the rib spacing on the mean and turbulent quantities for two different flow depths, $h = 45$ and 35 mm.
- To compare the present results with prior experimental and numerical studies conducted in fully developed channel and boundary layers.

CHAPTER 3

Principle and Implementation of Particle Image Velocimetry

3.1 Introduction

Particle image velocimetry (PIV) is a whole field, non-intrusive, quantitative, optical measuring technique. It can be used for the analysis of two-dimensional as well as three-dimensional flow fields. In this chapter, the basic principle of PIV is outlined and the various components of a PIV system are described.

3.2 Principle

The basic principle of PIV involves seeding the flow field with small tracer particles (seeding particles) that are assumed to faithfully follow the fluid motion. These seeding particles are then illuminated in a plane using timed laser pulses in order to visualize the fluid motion. Two images of the particles in the sheet are recorded in a short time interval. From their positions at the two instances of time, the particle displacements are calculated and the velocity field of the flow can be determined. The motion of the particles is usually recorded on either a photographic film or with a charged coupled device (CCD) camera. Compared to other flow measurement techniques, PIV is a multi-point technique and it is therefore very well suited for whole field measurements. Other attractive features of PIV include non-intrusive measurement and high accuracy, and as a result the technique has been applied in many areas of fluid mechanics. Detailed review of PIV technique can be found in Keane and Adrian (1990), Westerweel (1997) and Grant (1997). Figure 3.1 shows a schematic of a typical two-dimensional PIV system (the one used in the present

work). The system consists of a light source, a charged coupled device (CCD) camera, a buffer system and a computer with image acquisition software. The detailed description of various components of the PIV system is explained in the subsequent sections.

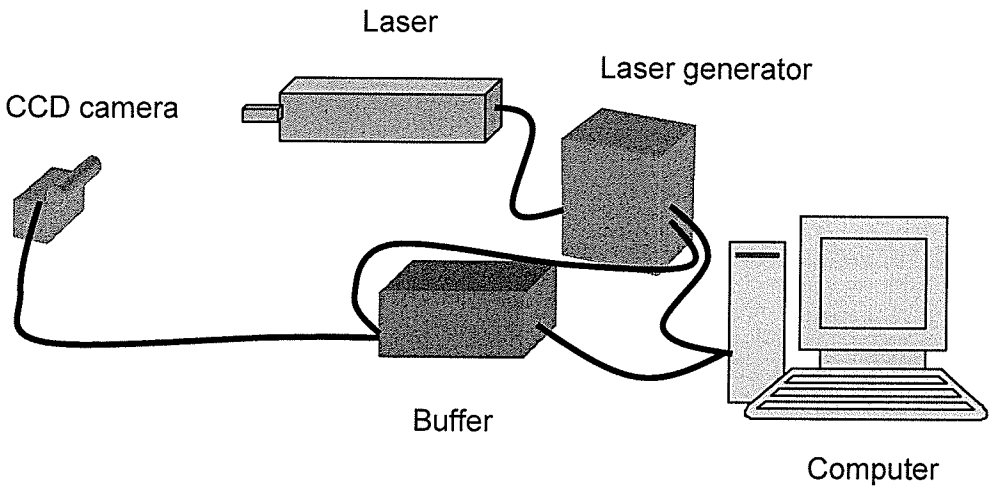

Figure 3.1: A typical experimental setup of a two-dimensional PIV system.

3.3 Light source

The light source for a PIV system should have high energy density and easy to convert into a thin sheet of light. Lasers are the most widely used light source for the PIV measurements because of their ability to emit monochromatic (single frequency) light with high intensity. Lasers have the special feature of eliminating chromatic aberrations while recording the light emitted by the seeding particles. For two-dimensional PIV, the plane of the light sheet is usually in the flow direction and at right angles to the camera's plane. A pulse light sheet is sometimes needed to freeze the motion of particles during image capture. Frequency-doubled Neodym-YAG (Nd: YAG) lasers are commonly used for PIV measurements to meet these requirements.

Continuous wave lasers such as He-Ne laser or Ar^+ laser can also be employed for PIV, however, they are usually used for low velocity measurements. Continuous laser has higher light intensity than pulsed lasers. However, the relatively lower power pulsed lasers do not have significant effect on performance because of the high sensitivity of CCD cameras used to register particles images. The lasers usually have a combination of a cylindrical and spherical lens that allows the thickness and orientation of the light sheet to be adjusted.

3.4 Seeding particles

PIV is an indirect velocity measurement technique. That is, it is the particle's velocity, not the fluid velocity that is determined by PIV. For accurate PIV measurements, the seeding particles should be distributed homogeneously (Westerweel, 1993, 1994) and should have the ability to follow the fluid faithfully without disturbing the flow of the fluid. Therefore, the hydrodynamic properties of the particles must be checked to ensure that the particles faithfully follow the flow. It is also necessary that the particles are small enough to follow the flow without disturbing it but large enough to scatter adequate light for them to be detected by the camera. A large difference between particle density, ρ_p, and fluid density, ρ_f, causes a settling velocity, v_s, which is not desirable. This settling velocity can be estimated from Stokes drag law for flow around a sphere. Mei et al. (1991) calculated the drag force on a sphere which states that a settling particle usually has a Reynolds number less than unity and the drag force on such a particle is given by

$$v_s = [(\rho_p - \rho_f)\, g\, d_p^{\,2}]/18\mu \qquad [3.1]$$

The particle Reynolds number is given by the following equation:

$$Re_p = [(\rho_f v_s\, g\, d_p)/\mu] \qquad [3.2]$$

In Equations [3.1] and [3.2], g is the gravitational acceleration, and μ is the velocity of the fluid. A particle's ability to follow the flow is characterized by its response time, which is a measure of the tendency of particle to reach the fluid velocity. The response time for a particle whose motion is governed by Stokes' law is given by (Westerweel et al., 1996):

$$\tau_R = (\rho_p v_s g d_p^2)/18\mu \qquad [3.3]$$

Since the particles must scatter enough light to make themselves visible to the CCD sensor, they must also be selected for their optical as well as hydrodynamic properties. Some important parameters in light scattering are the particle size and shape, the refractive index and the wavelength of radiation. Some of the seeding particles available for PIV range in size from a few microns to hundreds of microns, and are summarized in Table 3.1. The ultimate goal in particle selection is to obtain the most efficient scattering and maximize the light intensity of the sensor while minimizing settling. This is achieved by choosing small particles with density similar to the fluid density but large and polished enough to scatter light. The recommended minimum number of particles per interrogation area for cross-correlation and auto-correlation are five and ten respectively (Adrian, 1991).

Seeding particle	Mean particle diameter (μm)	Particle shape	Density (g/cm^3)	Refractive Index
Polyamide seeding particles	5, 20, 50	Non spherical	1.03	1.50
Hallow glass spheres	10	Spherical	1.1	1.52
Silver coated hallow glass spheres	10	Spherical	1.4	1.52
Florescent polymer particles	10, 30, 75	Spherical	1.5	1.68

Table 3.1 Recommended seeding particles for different studies

3.5 Recording medium

Before the advent of the electromagnetic imaging, photographic film was used for recording PIV images. The disadvantages such as lengthy iterative process to get the feed back of the recording and complex photo chemical processes have lead to the usage of electronic imaging. Out of many electronic sensors available today, the CCD camera is the most widely employed recording device for PIV. This is because of higher frame rates and possible on-line image analysis.

The main component of a CCD camera is the CCD sensor, which consists of a two-dimensional array of light sensitive picture elements called pixels. The electric charge on each pixel is proportional to the photon flux reaching the pixel and to the time the pixel is exposed to this flux. The charge of each pixel is read out at the end of each exposure. There are basically two types of CCD sensors: frame transfer sensors (FT) and the interline transfer sensors (ILT). A frame transfer sensor is composed of a

light sensitive pixel array and a storage array of identical size, which is shielded from the light. The charge of the pixels in the imaging array is transferred to the storage array after the pixels are exposed to the light. The transfer time is of the order of 0.5 to 1 ms. A new frame can be exposed while the previous one is being read out. The major advantage of frame transfer sensors is the concentration of all pixels on a small area and a minimum blind area (Spooren, 1994).

3.6 Methods of correlation and implementation

The images acquired by the CCD cameras are post processed using correlation analysis. The camera images are divided into small rectangular regions called interrogation areas or interrogation regions. For each of the interrogation areas, the images in the first and second pulse of light sheet are correlated to obtain an average displacement vector. Repeating the process for all the interrogation areas result in a vector map of average particle displacements. Dividing these vector maps of displacements with the time between the two images captured will produce a map of raw velocity vectors. To enhance the speed of the correlation, Fast Fourier Transformations (FFT) are generally used. By using FFT there will always be an output whether the input is meaningful or not. Therefore, it is necessary to validate the PIV vector map subsequently.

Basically there are two types of correlation techniques available. The first one is the auto-correlation and the second one is the cross-correlation/adaptive-correlation. Auto-correlation was the most widely used correlation technique in the past because of the difficulty associated with the separation of the initial and final particle positions on separate camera frames. In this technique the initial and final particle positions are recorded on the single frame. The image is correlated with the spatially shifted

positions of itself. Since the recorded image is correlated with itself, a large central peak is observed in the correlation plane corresponding to zero displacement along with two displacement peaks one each on either side of the central peak. This central peak is observed because of the seeding particles correlating with themselves and does not represent the zero velocity physically. The distance from the central peak (the self-correlation peak) to either of the displacement peaks is the average particle displacement in the interrogation area. One disadvantage associated with the auto-correlation is its low dynamic range. Because of the presence of the zero/self correlation peak, particle displacements less than 2-3 pixels can not be detected. Another major drawback in using the auto-correlation technique is its inability to identify the particle direction (180 degree directional ambiguity). This drawback makes its use limited to non re-circulating flows.

In cross-correlation technique, the particles in two different interrogation areas belonging to two different images are correlated. This method is more effective because the order of image recording is known, and therefore the direction of flow is unambiguous. In this technique the recorded two sequential images are sub sampled to form an array of regular two-dimensional interrogation areas. Within these interrogation areas, the seeding particles produce an average spatial shift from one image frame to its counterpart in the other image. As shown in Figure 3.2, the spatial shift can be represented by using a linear digital signal image process. The function f(m, n) describes the light intensity within the interrogation area at time t and the function g(m, n) describes the intensity recorded at time Δt later. The function f(m, n) is considered as the input signal and g(m, n) is the output of the transfer function s(m, n) in the presence of noise function d(m, n). The capitalized function shown in Figure 3.2 represents the Fourier transforms of the respective functions and u, v are the co-

ordinates of the spatial frequency domain. The challenge posed in this technique is to estimate the spatial shifting function s(m, n) on the basis of known functional values of f(m, n) and g(m, n) in the presence of noise function d(m, n). The details of statistical method used in estimating the spatial function s(m, n) is given in Willert and Gharib (1991) and Raffel et al. (1995).

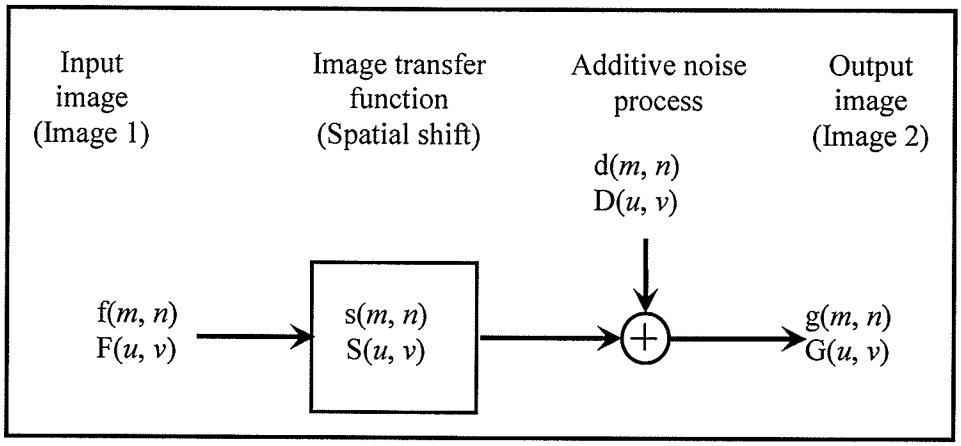

Fig 3.2 Image displacement function

There is also the adaptive-correlation algorithm, which is a special type of cross-correlation. The adaptive-correlation is fundamentally an iterative technique which relies on the knowledge of the actual velocity spatial distribution (which is not known a priori) and is the objective of the measurement procedure itself. Therefore, an initial guessed offset value is used to introduce an offset from the first window (the interrogation area in the image frame from laser pulse one) to the second window. The result of each single interrogation is used as an input to evaluate the interrogation parameters for the subsequent iteration. The process terminates when a convergence criterion is fulfilled or after a prescribed number of iterations. The main benefit

derived from using a shifted window (offset) is capturing the particle images that left the interrogation area during the time between the two light pulses. Loss of particle images reduce the signal strength and as a result, the number of successive vectors that can be obtained. The use of adaptive-correlation, therefore, helps in two ways. First, the signal strength is raised due to the capture of the loss particles. Secondly, a refinement of the interrogation area is possible because an adaptive window offset may be applied, again producing a successful signal.

Because of the advantage of cross-correlation over auto-correlation, the use of dual frame digital cameras (which are suitable for the correlation) has rendered the application of auto-correlation rare so the rest of the discussion will focus on the details of cross-correlation technique. The correlation function for integer pixel relative displacements is calculated by means of the FFT. The 2D FFT of each interrogation area is performed, and the element-by-element conjugate product is taken in Fourier space. The result is transformed backward using the inverse FFT algorithm. The highest peak in the resulting correlation surface indicates the relative displacement for which the best fit between image patterns was obtained, and is assumed to represent the real displacement.

Willert and Gharib (1991), however, identified errors and limitations that are intrinsic in this technique. They mentioned that FFT assumes the sample areas to be periodic in space and generates a circular form of cross-correlation, which does not fall to zero at the edges or the interrogation area. Figure 3.3 shows the numerical process chart of PIV. This consequently increases the background noise along the edges of the interrogation area. Also the size of the interrogation area limits the maximum detectable displacement. For large relative displacements the portions of overlapping interrogation areas become small and the signal to noise ratio diminishes.

Thus displacements larger than a quarter of the interrogation area size are not acceptable. There is, therefore, a compromise between the particle displacement and the spatial resolution achievable with this technique. Larger interrogation areas allow for larger particle displacement but lower spatial resolution since the displacement information is averaged over a larger portion of the flow field. Limitation on the maximum detectable displacement may be overcome by specifying a fixed offset between the first and the second interrogation areas. This may prove useful for flows with known mean velocity, but it should be noted that the maximum difference between detectable displacements remains unchanged. The above stated limitations of standard correlation algorithms can also be overcome by the adaptive-correlation technique mentioned earlier.

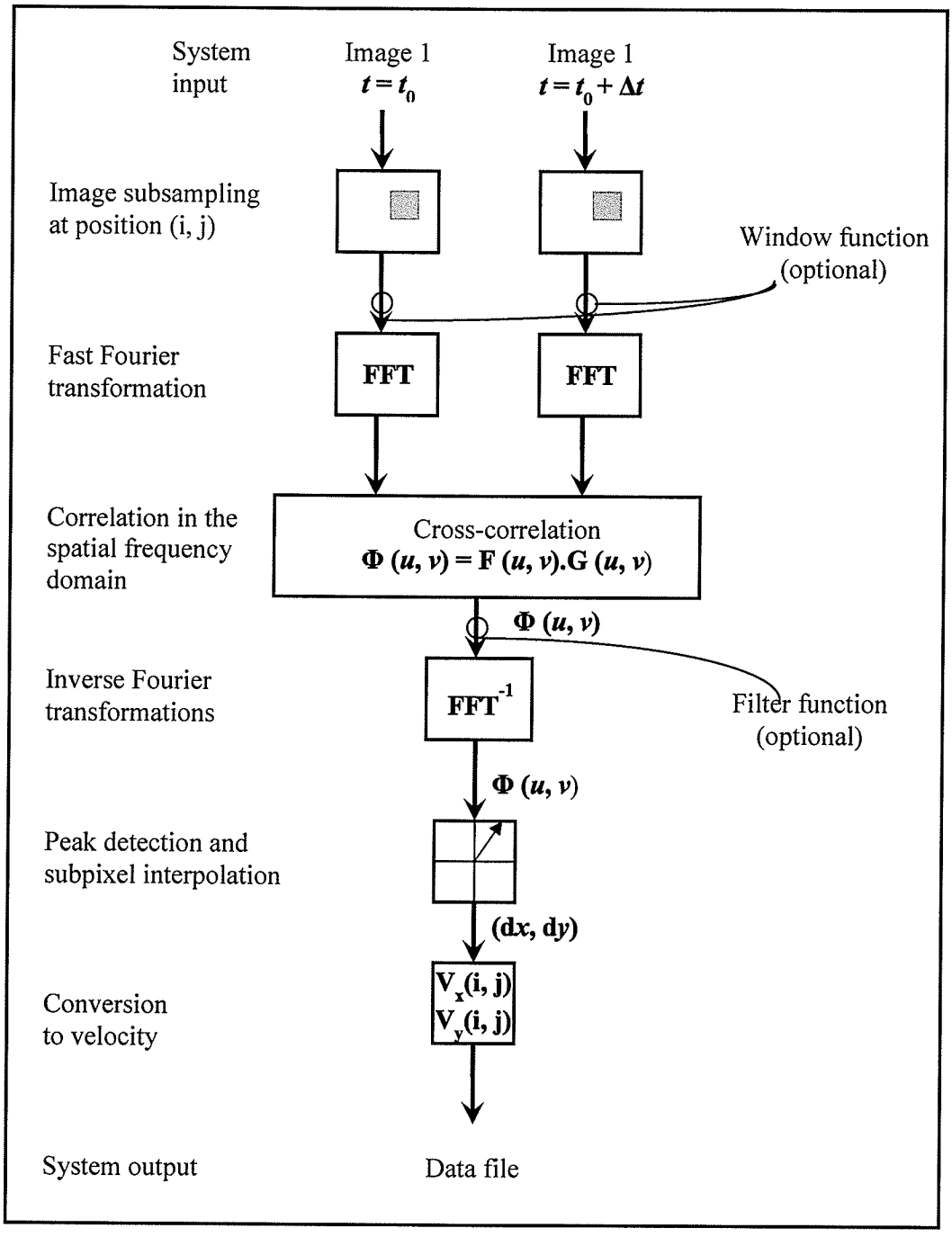

Fig 3.3 Numerical process flow chart of PIV

3.7 Optimizing PIV measurements

The combination of pulse separation time between successive pulses, laser energy, camera magnification and light sheet dimension needs to be optimized in order to obtain good results from a PIV system. Even when experimental conditions are ideal, a PIV vector map will contain spurious (false) vectors. These spurious vectors emanate from interrogation spots where signal to noise ratio is less than unity. That is, a noise peak is higher than the signal peak. Keane and Adrian (1990) focused their studies on the detection probability, that is, the percentage of valid vectors. To improve signal to noise ratio, they recommended the interrogation areas be large enough to accommodate a sufficient number of particles, but small enough so that one vector describes the flow. It was also recommended that the time separation should be set so that the variation in particle displacements within the interrogation cell is less than the particle image diameter. In order to make the images of a particle separable from one another they also recommended that the particles be allowed to travel more than one particle image diameter d_I given by

$$d_I = [d_p^2/S^2 + (2.44(1 + 1/S) f_\# \lambda)^2]^{1/2} \qquad [3.4]$$

where d_p is particle diameter, $f_\#$ is the f-number of the lens, λ is the wavelength of the laser light, and S is scale factor defined as the inverse of the magnification factor of the camera and lens arrangement. Keane and Adrian (1992) pointed out that when images are less than three pixel pitches in diameter there is insufficient information to make effective use of sub pixel interpolation because there is likelihood of biasing data towards integer pixel values. Therefore, the minimum time interval between images is

$$\Delta T \geq [d_I / Mu_{min}] \qquad [3.5]$$

where M is the image magnification and u_{min} is minimum velocity. The particle image density N_I is defined to be the average number of particle images within a square interrogation area with a size of L_I and is also given as

$$N_I = [(C_d L_I^2 \Delta z)/M^2] \qquad [3.6]$$

where Δz is the light sheet thickness, M is the image magnification and C is the seeding density of the particles within the flow and defined to be the number of particles per unit volume of the fluid. They showed that to obtain a high valid detection probability the particle image density should be larger than 6 for cross-correlation, however, it may be lower for adaptive correlation.

CHAPTER 4

EXPERIMENTAL SETUP AND MEASUREMENT PROCEDURE

This chapter details the experimental setup, data acquisition and processing and testing conditions.

4.1 Open-channel

The present study was performed in an open-channel. The water channel was designed and fabricated by Engineering Laboratory Design Inc., USA. The schematic of the open channel is shown in Fig. 4.1. The system is a recirculating design with the flow loop arranged in vertical configuration. The system includes a contraction section, test section, piping and supporting framework, filtering station, circulating pump and variable speed drive. The various sections of the water channel are discussed in the following sub-sections.

4.1.1 Test section

The sidewalls and floor of the test section are fabricated using super Abrasion Resistant (SAR) clear acrylic. The interior dimensions of the test section are 20 cm wide by 20 cm in height and 250 cm in length. Aluminum angle flanges, with threaded fasteners, join the test section to the contraction exit flange and return plenum entrance flange. Flow velocity in the test section can be varied between 0.2 m/s and 2.0 m/s.

4.1.2 Supporting framework

The supporting framework is made of structural steel tubing joined by welding to support the flow sections. The frames are etched, prime coated and spray finished with water-based acrylic enamel. The frame legs are fitted with adjustable leveling pads. Vibration pads are located at contact points with the ducts to isolate the system from vibration. The PVC piping is used throughout and the mating flanges and pipe saddle floor supports are also fabricated from PVC. Flexible rubber couplings are used to join the piping to the flow sections and will isolate the pump from the main components of the tunnel.

4.1.3 Pump and motor

A closed impeller centrifugal pump (Flow serve Model No.6X4X10 GRP) was used. The pump case and impeller are fabricated from a GRP and the shaft is fabricated of type 316 stainless steel. The pump is belt driven by a 25 HP, TEFC, 1750 RPM, 600V AC (3 phase and 60 Hz) motor (US Motors Model No.T627). The pump and the motor sheave ratio are arranged such that the pump can operate at a maximum of 1600 RPM. The pump shaft's RPM is regulated by a 25 HP transistor inverter type variable speed controller (Toshiba Model No. VT130H746270).

4.1.4 Filter station

Dye concentrations and other contaminants are filtered from the system water using a 1/20 HP circulating pump (Laing Thermotech Model No. SM-909-BF-18). The filter station has stainless steel filter housing and replaceable activated carbon particle filter cartridges. The filter station can approximately filter 833 liters of system water in approximately one hour period.

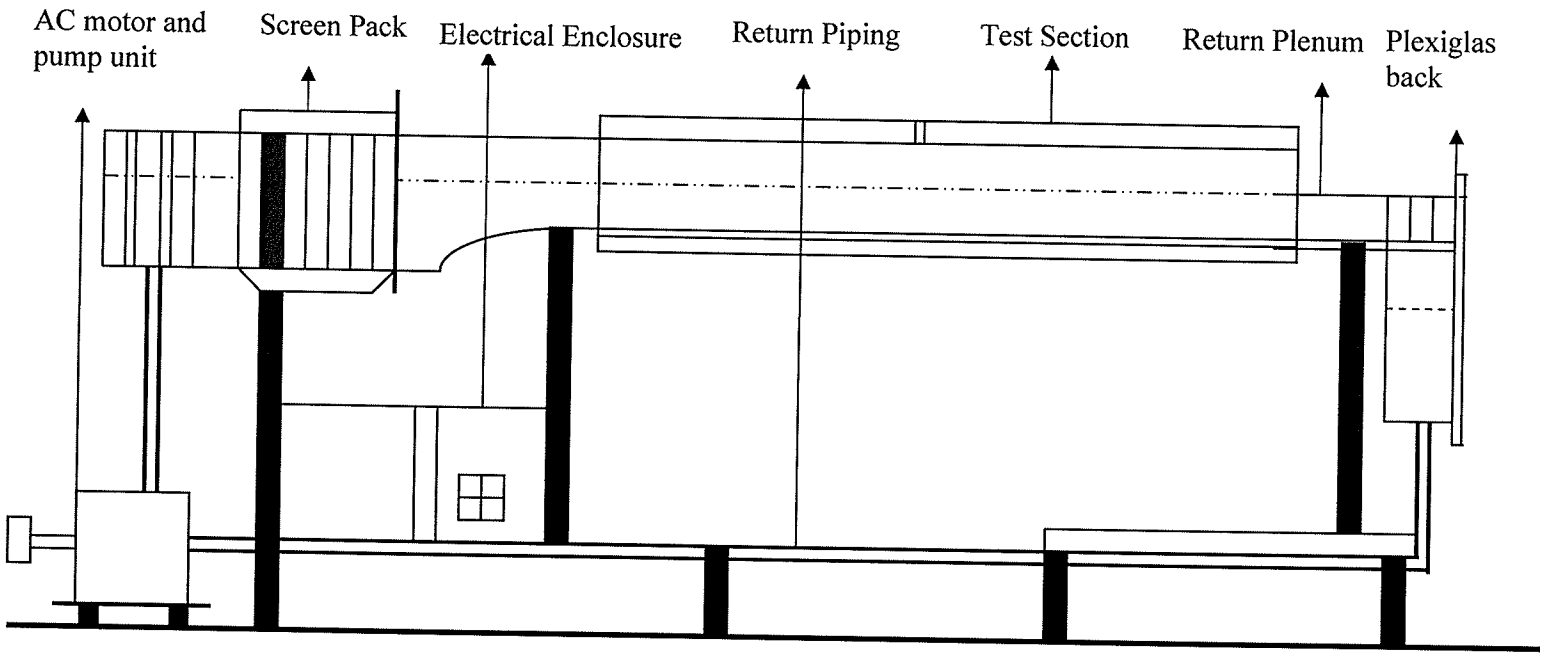

Fig. 4.1 A schematic diagram of water tunnel facility.

4.2 Roughness models

Roughness models are created by arranging 6 mm square cross-sectioned acrylic rods on the bottom wall of the channel. The acrylic rods are hereafter termed as ribs for convenience. The ribs were glued on a 4-mm plexiglas sheet that spans the entire width and length of the channel using a double sided tape. The sheet was then tightly screwed onto the bottom wall of the channel. The ribs are spaced uniformly in every model. The spacing between the ribs or pitch (p) is varied to produce three different types of roughness. More specifically, pitch values of 12 mm, 24 mm and 48 mm were used to obtain d-type (p/k = 2), intermediate (p/k = 4) and k-type (p/k = 8) rib-roughness, respectively. The three rib type dimensions are shown in Figure 4.2. The ribs are arranged on the bottom wall starting at 1400 mm from the inlet of the test section. For d-type roughness model, 40 ribs are arranged on the bottom wall of the channel and the number of ribs used for the intermediate and k-type roughnesses are 20 and 10, respectively.

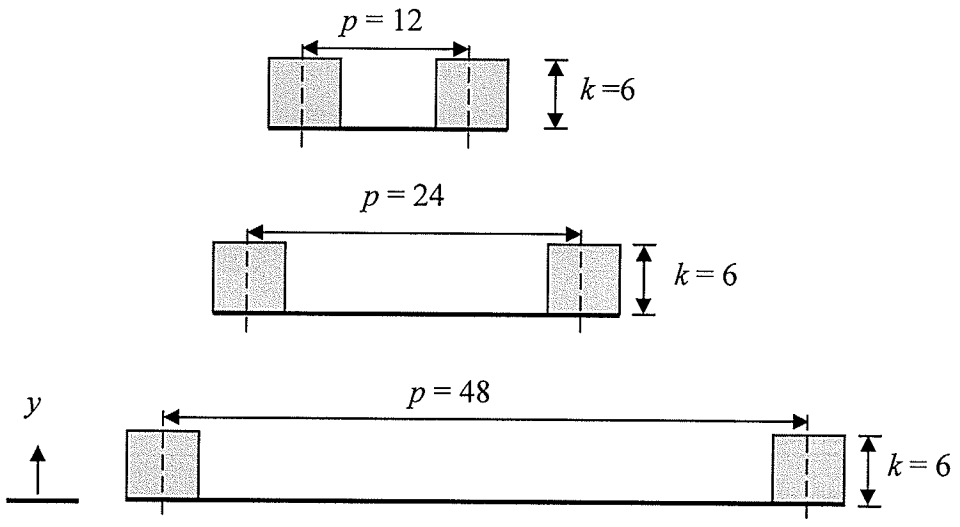

Fig. 4.2 Dimensions of d-type, intermediate and k-type ribs used in the present study. All dimensions are in mm.

4.3 Particle image velocimetry (PIV)

Figure 3.1 illustrates the details of the PIV system used for the present study. A double pulsed Nd: YAG laser (New wave Research Inc.), which can deliver laser pulses at a wavelength of 532 nm with a maximum energy of 120 mJ per pulse at a frequency of 15 Hz, was used. A high resolution digital camera (Dantec Dynamics Inc.) which uses a charged coupled device (CCD) of 2048 x 2048 pixel chip was employed for recording the flow filed. The camera has a 60 mm diameter Nikkon lens and the pixel pitch of the CCD chip was 7.4 μm. Commercial software (Flow manager version 4.5) installed on a 1 GB RAM of the Dell Pentium IV computer was used for the data acquisition and post processing of the acquired data. A synchronizer integrated in the software synchronizes the camera and laser, and a buffer system was used to enhance rapid transfer of the digital images from the camera to the computer.

The flow was seeded with polyamide seeding particles (PSP) of mean diameter 5 μm. The seeding particles chosen for the present study (PSP) have a specific gravity of 1.03, which is very close to the specific gravity of water. The settling velocity and response time of the particles were estimated to be 0.41 μm/s and 1.43 μs, respectively. The settling velocity is very small compared to the mean axial velocity measured and the particle response time is very small compared to the time interval between exposures, Δt, of about 250 μs so that the particles are considered to follow the fluid faithfully. The particle displacement during the sampling period was about 85 μm. This displacement is greater than 3 times the diameter of the pixel ($\approx$ 25 μm) and about a quarter of the interrogation area ($\approx$ 100 μm). Thus the chosen data acquisition system and the process

parameters satisfy the condition for minimum and maximum particle displacements discussed earlier in Chapter 3.

The CCD camera was fitted to a C-mount lens with a green filter (cut-off wavelength is 532 nm) that allows only light scattered by the seeding particles into the camera. The camera was mounted on a traversing mechanism to facilitate adjustment during focussing. In a PIV technique, a calibration is required to establish a relationship between pixel displacements (on the CCD camera) and flow displacement in physical units (mm). This relationship is termed the scale factor. In this study, a thin metallic ruler (0.5 mm thick) was used to calibrate the system. During the calibration process, the ruler was positioned at the measurement locations of interest inside the channel. The camera lens was then adjusted until the graduation on the ruler was well focussed. The PIV software was used to complete the calibration process and the scale factor obtained. A typical scale factor was 3.401, and the camera's field of view was determined after the calibration to be approximately 51.5 mm × 51.5 mm. Different focal numbers on the camera were used to take images and from the processed images it was found that focal number values greater than 10 gave good background contrast. All measurements reported in this study were made using $f_{\#} = 16$ because apart from having the best contrast, it also provided particle image sizes large enough to meet the requirements listed earlier in Chapter 3.

4.4 Test conditions and measurement procedure

Figure 4.3 shows a schematic of experimental setup and also define the co-ordinate system used in this study. Here the streamwise, wall-normal and spanwise directions are denoted by x, y and z respectively; $x = 0$ corresponds to the upstream edge of the first rib, $y = 0$ corresponds to the floor of the channel (Plexiglas sheet) and $z = 0$ corresponds to the middle plane of the channel. The flow was tripped using a 40 mm wide strip of 1-mm sand grains spanning the width of the channel was placed 100 mm from the entrance of the channel to enhance a rapid development of the boundary layer. As mentioned earlier in section 4.2, the measurements were made over three different rib configurations, namely d-type, intermediate and k-type rib-roughness. The ribs were arranged on the channel floor starting at 1400 mm from the inlet of the test section to about 1900 mm from the inlet of the test section. For d-type ribs ($p/k = 2$), 40 ribs were arranged at equal pitch on the channel floor. The number of ribs arranged for intermediate and k-type roughness were 20 and 10, respectively. Preliminary measurements were made to study the flow development over the ribs. Form these results it was decided to conduct all subsequent measurements beyond the 5^{th} rib that is, $x/k > 4$. In these experiments, 2500 images were recorded. From these images, the time averaged mean velocity and turbulent statistics were calculated from the following number of samples or images: N = 500, 1000, 1500, 2000 and 2500. It was observed that the mean quantities obtained using 1000 samples or more collapse within measurement uncertainty. This suggests that 1000 images are adequate to obtain converged mean velocities. It was found that 2000 images are necessary to obtain converged turbulent quantities. Based on these results, all the mean velocity and turbulent quantities reported in this work were obtained using a

sample size of 2500. For each roughness configuration, measurements were made at two different water heights, h = 35 mm and 45 mm. All the measurements were taken in x-y plane for z = 0 (central plane) position. The freestream velocity of approach boundary layer was kept constant in all experiments. Measurements were also taken over smooth channel ($\approx$ 250 mm up-stream of the first rib) approximately 1150 mm from the entrance of the test section. This is necessary to document the characteristics of the approach boundary layer.

Table 4.1 summarizes the test conditions. In this table, h is the height of the water column, p is the center to center spacing between adjacent ribs, k is the height of the rib, U_e is the freestream velocity, δ is the boundary layer thickness, θ is the momentum thickness, Re_h (= $U_e h/\nu$, where ν is kinematic viscosity) and Re_θ (= $U_e\theta/\nu$) are Reynolds numbers based on height of the water column and momentum thickness, respectively, and Fr, is the Froude number. The Froude number is defined by the following relation, $Fr = U_e/(gh)^{1/2}$, where g is the acceleration due to gravity.

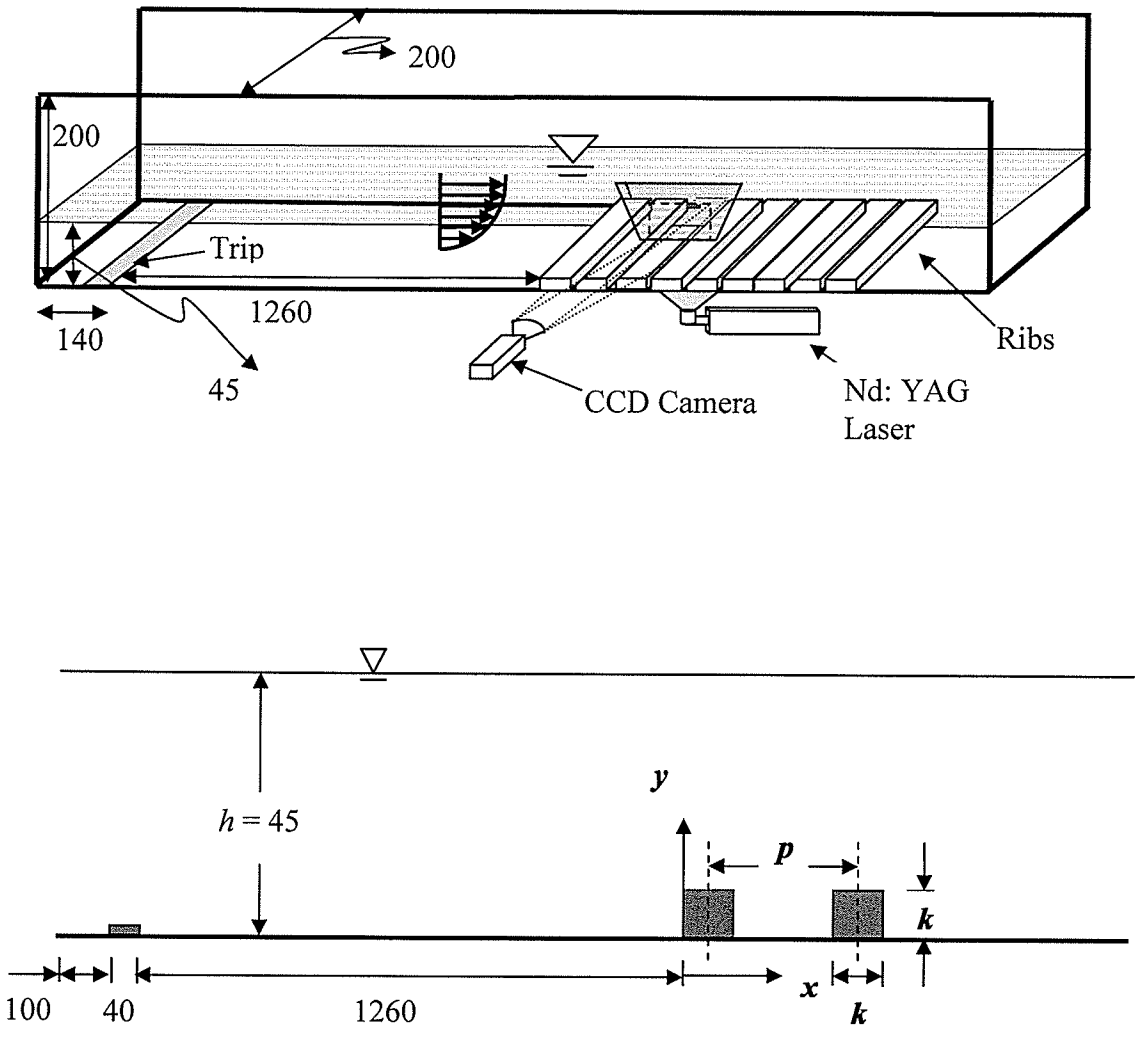

Fig. 4.3 A Schematic diagram of experimental setup showing the test section and co-ordinate system. All dimensions are in mm

h (mm)	*Surface type*	p (mm)	k (mm)	U_e (m/s)	δ (mm)	θ (mm)	Re_h	Re_θ	Fr
45	*SM*	--	--	0.21	36.6	3.71	9,000	790	0.30
	d-type ribs	12	6	0.26	36.6	3.75	11,700	975	0.39
	intermediate ribs	24	6	0.26	38.2	4.14	11,700	1080	0.39
	k-type ribs	48	6	0.29	38.2	4.92	13,050	1430	0.43
35	*SM*	--	--	0.21	22.9	2.14	7,350	450	0.36
	d-type ribs	12	6	0.26	31.4	2.17	9,100	570	0.44
	k-type ribs	48	6	0.29	31.4	3.77	10,150	1100	0.49

Table 4.1 Boundary layer and rough-wall parameters

4.5 PIV data processing

Fig. 4.4 shows a sample PIV image and its corresponding streamlines pattern. The acquired digital images in PIV experiments were post processed using an adaptive-correlation algorithm (details given in Chapter 3) in-built in Flow manager software. Every image was subdivided into 32 x 32 pixel interrogation areas and an overlap of 50% was used for the post processing. The selected interrogation area and the overlapping provide a spatial resolution of 0.40 mm x 0.40 mm with at least 6 particles in every interrogation area of the PIV image.

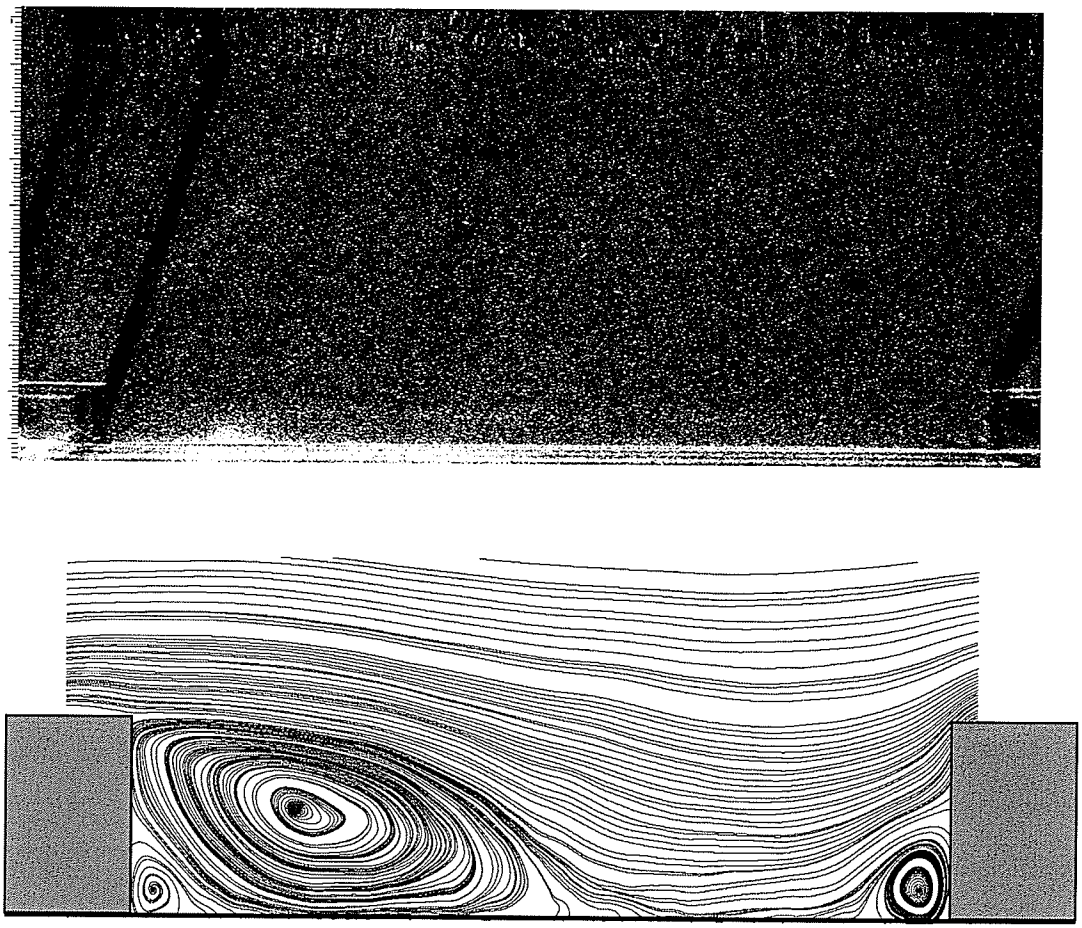

Fig. 4.4 Sample PIV image and its streamlines pattern

4.6 Measurement uncertainty

A detailed uncertainty analysis was performed following the procedure illustrated by Coleman and Steele (1995). Measurement errors arise from various sources but the total uncertainty (E) in PIV can be broadly categorized into a bias component (B) and a precision component (P). The main source of bias errors in PIV is calibration procedure. The bias limit of the measured velocity is determined with a root-sum-square (RSS) of

the elementary bias limits (B_x) based on the sensitivity coefficients given as (Coleman & Steele, 1995)

$$B_U = \theta^2_{L_O} B^2_{L_O} + \theta^2_{L_I} B^2_{L_I} + \theta^2_{\Delta s} B^2_{\Delta s} + \theta^2_{\Delta t} B^2_{\Delta t} \qquad [4.1]$$

where the sensitivity coefficients θ_x are defined as $\theta_X = \partial U/\partial X$, $X = (L_0, L_I, \Delta t, \Delta s)$. The classification of bias error sources and contribution to the bias limits for (U) are provided in Table 4.2 together with the manufacturer's specifications of the elementary bias limits for Δt and Δs.

The precision errors, on the other hand, result from scatter in the measured data. Variations of measured quantities and operating conditions are some of the factors that influence precision errors. Precision errors are estimated statistically from the relation $P_x = K.\ \sigma$, where K is the confidence coefficient and has a value of 2 for a 95% confidence level for sample size $N > 10$ and σ is the standard deviation of the sample of N readings of the variable X, and is defined as

$$\sigma = \sqrt{\frac{1}{N-1}\sum_{k=1}^{N}\left(X_k - \overline{X}\right)^2} \qquad [4.2]$$

where $\overline{X}$ is defined by

$$\overline{X} = \frac{1}{N}\sum_{k=1}^{N} X_k \qquad [4.3]$$

The total uncertainty, E, is obtained from the square root of the sum of the squared uncertainties as $E_X = \sqrt{B_X^2 + P_X^2}$.

Variable	Magnitude	B_x	θ_x	$(B_x*\theta_x)$	$(B_x*\theta_x) / \Sigma (B_x*\theta_x)$	$(B_x*\theta_x)^2$
L_o (m)	5.150E -02	1.000E -04	6.146E +00	6.146E -04	-4.878E -07	3.777E -07
L_1 (pix)	2.048E +03	5.000E -01	-1.545E -04	-7.727E -05	6.134E -08	5.971E -09
Δt (s)	2.500E -04	1.000E -07	-1.266E +03	-1.266E -04	1.005E -07	1.603E -08
Δs (pix)	3.14668	1.573E -02	1.006E -01	1.583E -03	-1.256E -06	2.504E -06
		Sum	-1.260E +03			2.904E -06
			Velocity	0.19782		
			Std. Deviation	0.0097698		
			Bias Error	0.0017042		
			Bias Error (%)	0.861477		
			Precision Error	0.0195395	0.0987743	
			Total Error (%)	0.86712106		

Table 4.2 Bias and precision limits of mean velocity in rib roughened region

The uncertainty in mean velocity, turbulent intensity and Reynolds shear stress are estimated to be 1%, 5% and 7.5% for rib-roughened region as well as smooth-wall regions respectively.

CHAPTER 5

RESULTS AND DISCUSSIONS

5.1 Introduction

In this chapter the results obtained over the smooth-wall and the three rib types for the two depths of water column (h = 45 mm and h = 35 mm) are presented and discussed. The results obtained in the present study are also compared with prior experimental and numerical studies.

5.2 Smooth-wall profiles

To facilitate a good understanding of the effects of the rib-roughness on the mean and turbulent quantities, it is customary to compare the results obtained on the rib-roughened walls with corresponding smooth-wall results. As mentioned in Chapter 4, the smooth-wall data were obtained at 250 mm upstream of the first rib (x = - 250 mm). In this section the streamwise mean velocity, turbulent intensities and Reynolds shear stress profiles over the smooth-wall for h = 45 mm and h = 35 mm are discussed and compared with previous LDA measurements obtained by Tachie et al. (2003) in an open-channel turbulent boundary layer. The Reynolds number based on momentum thickness in the LDA study was Re_θ = 1900, which is more than twice the values obtained in the present study. All profiles in this section are normalized by outer co-ordinate scaling (U_e and h).

Fig. 5.1(a) shows the streamwise mean velocity profiles. The normalized values observed for h = 45 mm appears to be slightly lower than h = 35 mm for $y/h < 0.7$ and collapsed on each other beyond this range. This difference may be due to the slight variations in the Reynolds number and possible experimental errors. It can be observed

from Fig. 5.1(a) that the present profiles collapse reasonably well with the profile of Tachie et al. (2003). The distribution of the streamwise turbulent intensity is shown in Fig. 5.1(b). It is clear from this figure that the profiles for h = 45 mm and h = 35 mm show a peak very close to the wall and decreases gradually towards the freestream. The peak value observed for both profiles is approximately $(u/U_e)_{max}$ = 0.13. The profiles obtained in the present study collapse reasonably well on to each other. Close to the wall and the freestream, the present profiles are in good agreement with the LDA data by Tachie et al. (2003). However for $0.2 < y/h < 0.6$, the values reported in Tachie et al. (2003) are slightly higher than in the present study. This disparity observed in the profiles can be attributed to the Reynolds number difference in the two studies. Fig. 5.1(c) shows the distribution of wall-normal turbulent intensity. The trend observed in this case is very similar to the streamwise turbulent intensity, but the peak value observed in this case is relatively smaller $(v/U_e)_{max} \approx 0.045$ for both profiles, h = 45 mm and h = 35 mm. The profiles also show a reasonably good collapse across the entire depth. Comparison with the previous LDA result reveals that the previous values are slightly higher than in the present study. However, these differences are within measurement uncertainty. Fig. 5.1(d) shows the Reynolds shear stress profiles. These profiles show higher Reynolds stress values close to the wall and decrease smoothly towards freestream. The peak value observed for both profiles in the present study is approximately $(-\langle uv \rangle/U_e^2)_{max}$ = 0.0015. Close to the wall, the agreement between the present study and previous results of Tachie et al. (2003) is good. However, the previous results are slightly higher compared to the present study away from the wall. Again the difference in Reynolds numbers might be the reason for the disparity.

Though there are slight variations in the streamwise velocity profiles for h = 45 mm and h = 35 mm, turbulent quantities show a reasonable collapse. These results support the conclusion that the height of water column has no significant impact on the smooth channel results. Taking into consideration the differences in the Reynolds numbers in the present and prior study of Tachie et al. (2003) and also experimental errors, it can be concluded that the present results are in reasonable agreement with those obtained in the earlier study.

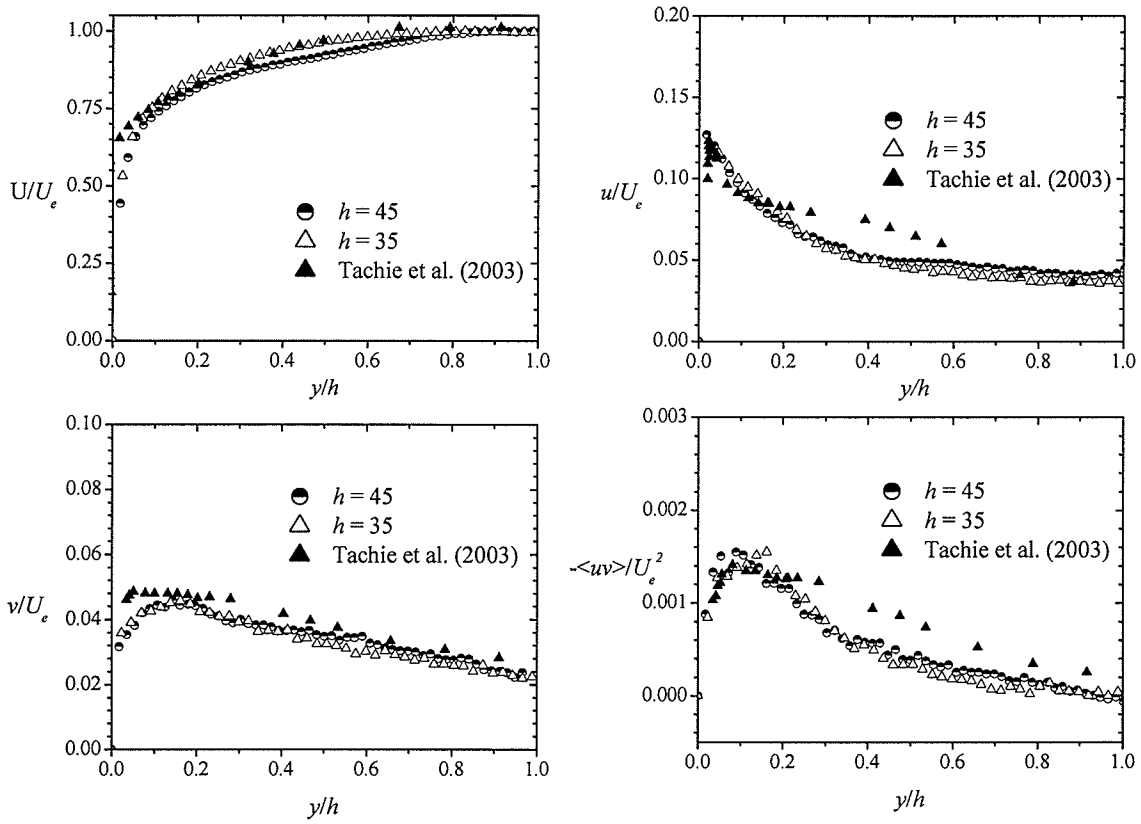

Fig. 5.1 Smooth wall profiles (a) streamwise mean velocity; (b) streamwise turbulent intensity; (c) wall-normal turbulent intensity; (d) Reynolds shear stress.

5.3 Rib-roughness

In this section the results for h = 45 mm and 35 mm over the d-type, intermediate and k-type ribs are presented. Typical velocity vectors, streamlines and vorticity contours obtained over the ribs are shown. For all the three rib types, profiles obtained at the center or crest of ribs 6 and 7, and at various locations in the cavity between these two ribs are plotted. For the d-type and intermediate ribs, additional data sets were obtained in the cavity upstream of rib 6 and downstream of rib 7. In the following section, profiles obtained at the center or crest of the ribs will be referred to as rib-tops.

5.3.1 Vector and streamline diagrams

The velocity vectors inside and above the cavities for the three roughness configurations considered in the present study are shown in Fig. 5.2. These velocity vectors show the variation of mean velocity in the flow direction (x-direction). To present the data clearly some vectors are skipped in every case. Some of the velocity vectors inside the cavities move in opposite direction to the flow, indicating negative velocities. Since the ribs were closely placed for d-type roughness (Fig. 5.2a), there is only a small cavity between the crests of the ribs. The magnitude of the negative velocities observed in d-type cavity is very small compared to intermediate and k-type cavities. The velocity vectors for d-type and intermediate ribs become parallel to the main flow just above the crests of the ribs. However the mean flow over k-type ribs is remarkably inhomogeneous so that the vectors remain unparallel to a greater distance above the ribs (approximately two rib heights distance above the crests of the ribs).

Fig. 5.3 shows the streamlines pattern for the three rib configurations considered in the present study. For *d*-type ribs, a small stable vortex fills the cavity between the adjacent ribs. Incase of the intermediate ribs, the cavity between adjacent ribs is occupied by a large stable clockwise rotating vortex and a small counter rotating vortex just behind the upstream rib. These stable vortices in the *d*-type and intermediate cavities prevent the outer flow from reattaching onto the channel floor within the cavity. For the *d*-type and intermediate ribs, the streamlines beyond the rib height are nearly parallel to the outer flow. On the other hand, streamlines for *k*-type ribs show a large stable clockwise rotating vortex and two counter rotating small vortices. The counter rotating vortices are observed adjacent to upstream as well as downstream ribs. The outer flow reattaches to the floor between the ribs at about four times the rib height from the upstream rib. Consistent with observations made in Fig. 5.2(c), streamlines above the ribs are non parallel up to approximately two rib heights distance (the exact distance is not shown in Fig. 5(c)) due to stronger interaction between the outer flow and cavity of *k*-type ribs. The streamlines obtained in the present study are qualitatively similar to LES results of Cui et al. (2003). The reattachment length obtained in the present study also agrees well with the LES result of Cui et al. (2003). The reattachment phenomenon observed for *k*-type cavity is also consistent with the prior LES results of Cui et al. (2003) with one wall roughened by square ribs and also DNS results of Leonardi et al. (2003).

Fig. 5.4 shows isocontours of the mean spanwise vorticity ($\Omega_z = \partial V/\partial x - \partial U/\partial y$) for the three rib configurations. The figure reveals regions of intense shear layer in the vicinity of the ribs. Because $\partial V/\partial x < \partial U/\partial y$, values of Ω_z are negative everywhere. The bulk of vorticity is generated above the ribs and convected downstream into the cavity.

Inside the cavity, more intense vorticity is found for *d*-type ribs than for intermediate and *k*-type ribs. As previously mentioned for *d*-type cavity the interaction between the outer flow and the cavity is negligible. As a result, the mean velocities in the wall-normal direction are negligible in the cavity ($V \approx 0$). Therefore the mean vorticity simplifies to $\Omega_z \approx - \partial U/\partial y$.

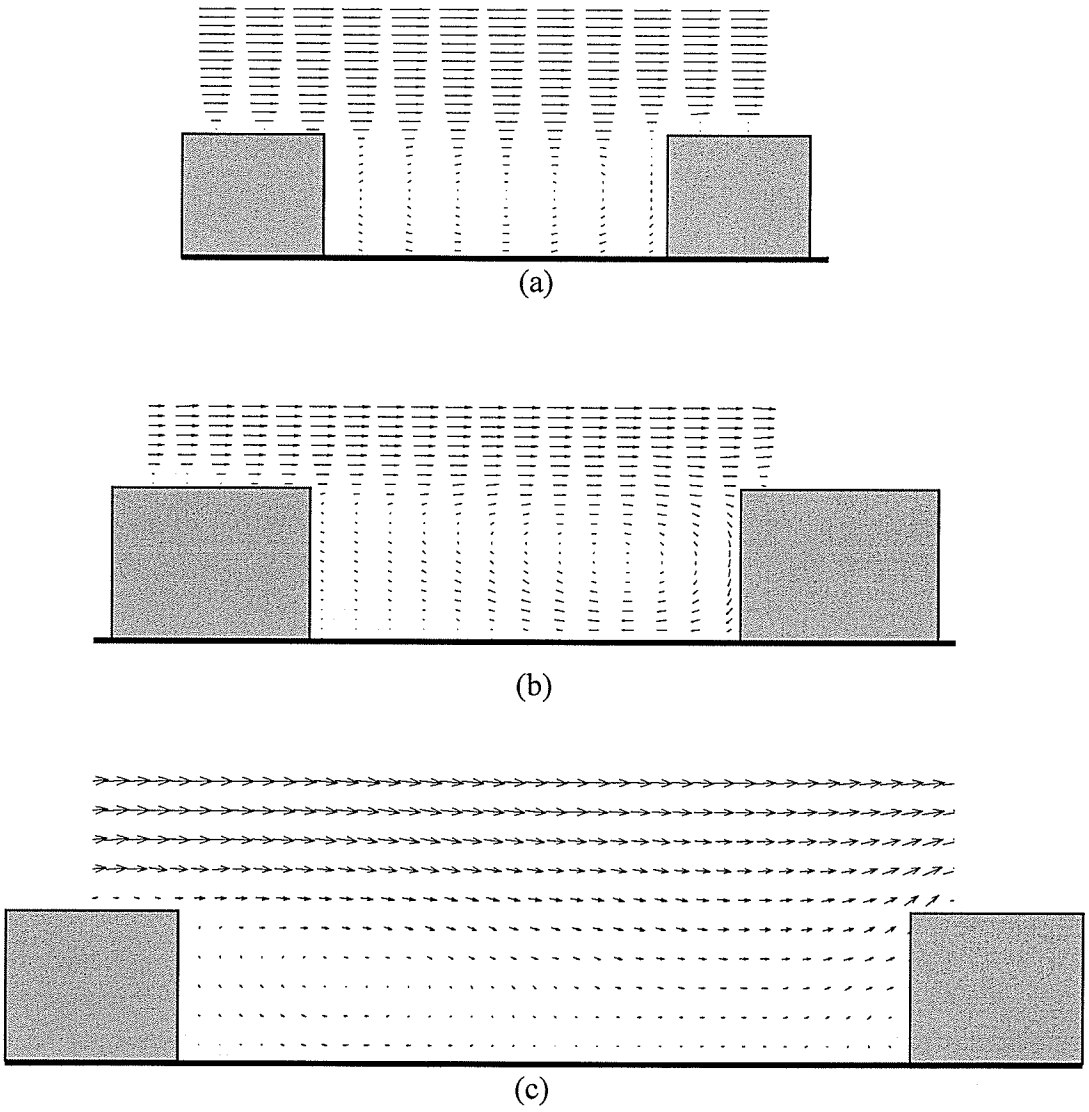

Fig. 5.2 Velocity vectors inside and above cavity (a) *d*-type; (b) intermediate; (c) *k*-type ribs.

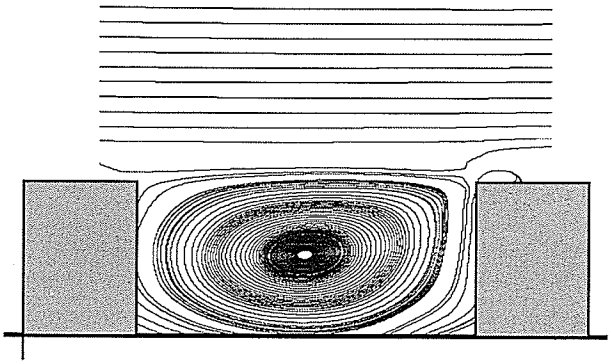

(a)

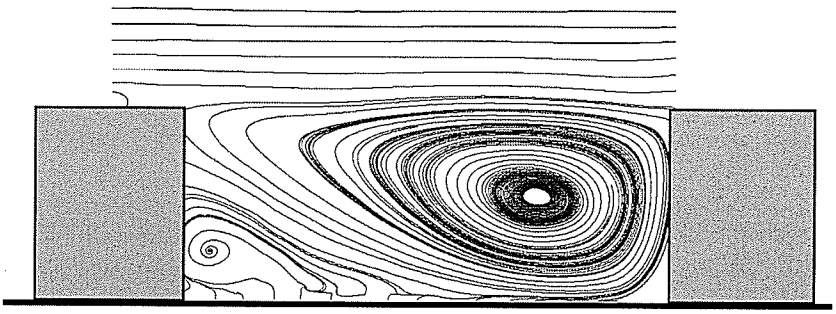

(b)

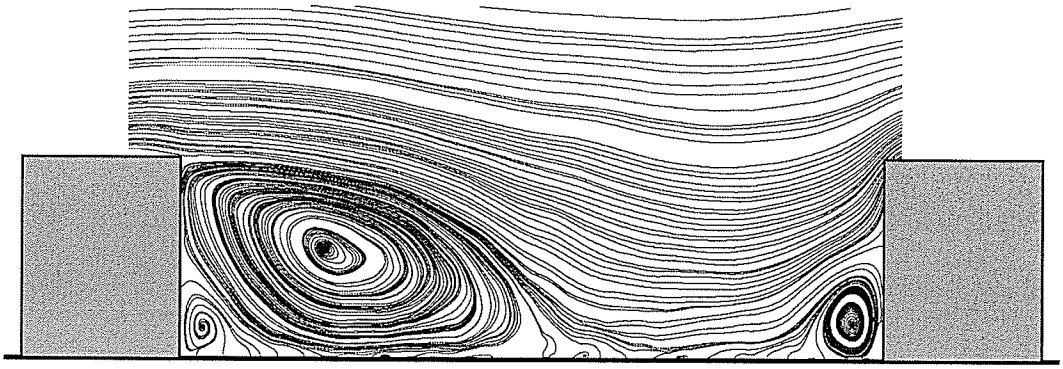

(c)

Fig. 5.3 Streamlines inside and above cavity (a) *d*-type; (b) intermediate; (c) *k*-type ribs.

(a)

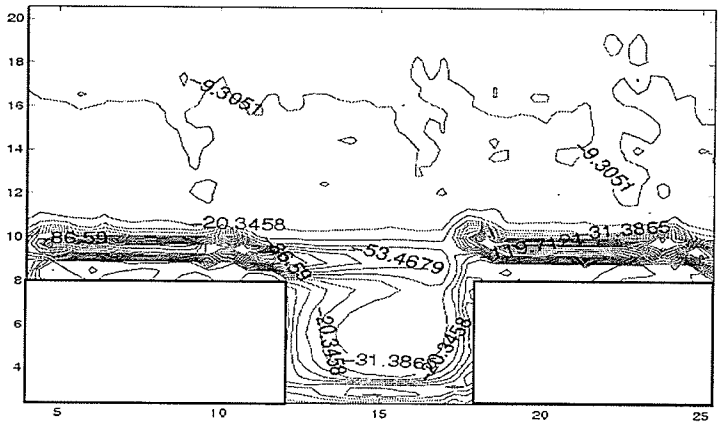

(b)

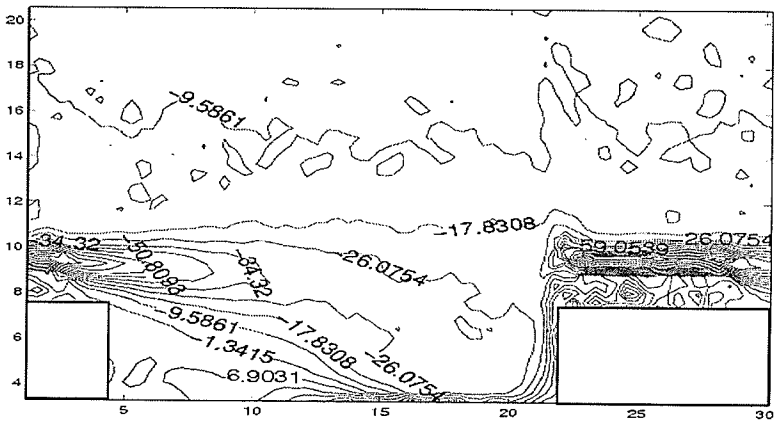

(c)

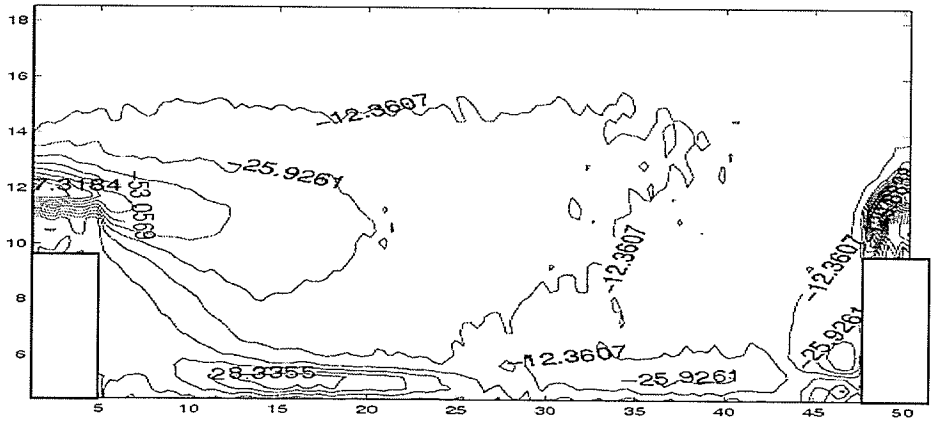

Fig. 5.4 Isocontours of mean spanwise vorticity inside and above cavity: (a) *d*-type; (b) intermediate; (c) *k*-type ribs.

5.4 Mean velocity and turbulent quantities

5.4.1 Mean velocity profiles

The streamwise mean velocity profiles for h = 45 mm and 35 mm are shown in Figs. 5.5 and 5.6. The velocity, U, and wall-normal distance relative to the floor, y, are normalized by the freestream velocity, U_e, and the water depth, h, respectively. The profiles are terminated at $y/k = 6$ (or $y/h = 0.8$) for h = 45 mm and at $y/k = 5$ (or $y/h = 0.85$) for h = 35 mm because data beyond these points do not provide any valuable information. The dash lines correspond to the top plane of the ribs. In this and subsequent figures, different axial locations are denoted as multiples of rib height, k. The data presented in this and subsequent sections over d-type, intermediate and k-type ribs fall between the axial locations $9 \leq x/k \leq 13$, $18 \leq x/k \leq 24$ and $40 \leq x/k \leq 48$, respectively. The axial location for the crest of any rib (d-type, intermediate and k-type) is a whole multiple of that pitch ratio (p/k) and are denoted by open symbols. All other locations correspond to cavities. The cavity centers are denoted by solid symbols. For example, the axial location $x = 20k$ corresponds to the crest of rib numbered 6 for intermediate roughness (because axial location $20k$ corresponds to intermediate rib and it is also a whole multiple of 4), $x = 43k$ corresponds to the cavity between ribs numbered 6 and 7 for k-type roughness (because the axial location $43k$ corresponds to k-type rib and is not a whole multiple of 8).

The magnitude of the negative velocity observed in the cavities increases with p/k. The maximum negative velocity observed is about 15% of the freestream velocity for k-type ribs, 5% for intermediate ribs and only 1% for d-type ribs. Figs. 5.5(a) and 5.6(a) reveal that profiles obtained at various locations within the cavities of d-type ribs collapse reasonably well irrespective of the water depth (h = 45 mm and h = 35 mm). The profiles

over *d*-type rib-tops also collapse reasonably well. The profiles in the cavities and over the rib tops are similar in the region $y/k > 4$ for $h = 45$ mm and $y/k > 3.5$ for $h = 35$ mm. For the intermediate ribs, Fig. 5.5(b) shows that profiles at adjacent rib-top locations ($x/k = 20$ and 24) are nearly indistinguishable right from the rib-top. But inside the intermediate cavity, the profiles at different axial locations are slightly different. For example, the maximum negative velocity is higher at center of the cavity ($x/k = 18$, 22) than other cavity location ($x/k = 19$, 23). Though there are slight variations in the velocities inside the cavity, these profiles collapsed onto each other just above the rib height. As shown in Figs. 5.5(c) and 5.6(c), for *k*-type ribs the profiles at the rib-top locations ($x/k = 40$, 48) show slight differences up to $y/k \approx 2$, and are nearly indistinguishable thereafter. However, inside cavity, the profiles corresponding to various axial locations differ significantly, and the maximum negative velocity is observed ahead of center of cavity. This is because the center of vortex is shifted upstream of the geometric center of the cavity due to reattachment of the flow on the floor inside the cavity. This phenomenon is observed for both $h = 45$ mm and $h = 35$ mm profiles. Though profiles corresponding to various axial locations inside the cavity differ, a good collapse of all cavity and rib-top profiles is observed for $y/k > 4$.

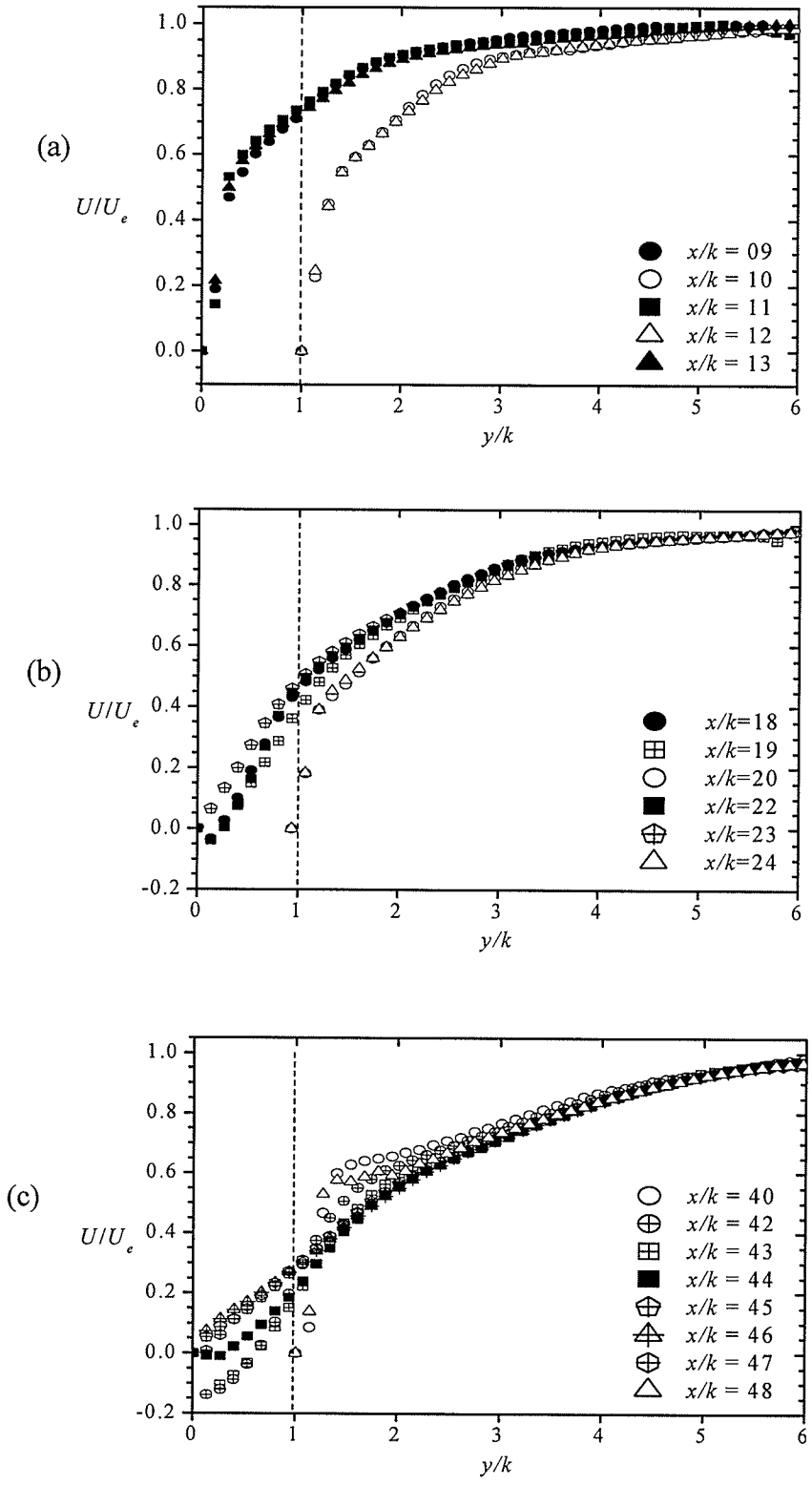

Fig. 5.5 Mean velocity profiles normalized by freestream velocity over (a) *d*-type; (b) intermediate; (c) *k*-type ribs for $h = 45$ mm

(a)

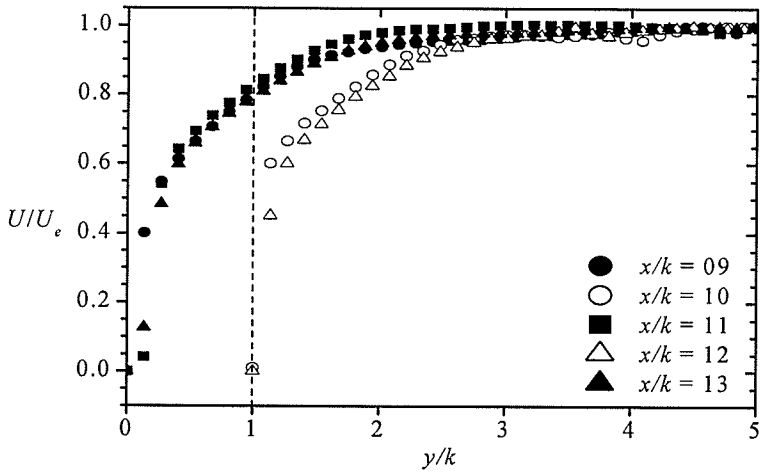

(b)

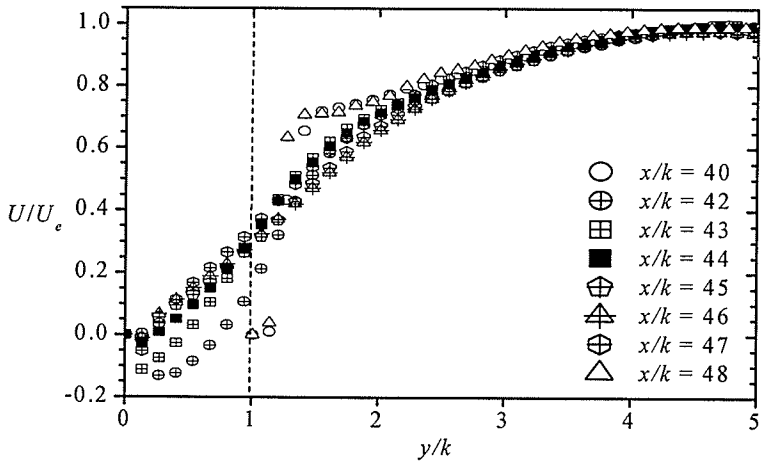

Fig. 5.6 Mean velocity profiles normalized by freestream velocity over (a) *d*-type; (b) *k*-type ribs for $h = 35$ mm

Fig. 5.7 shows the streamwise mean velocity profiles for the present *d*-type, intermediate and *k*-type cavities and those obtained in earlier studies. Fig. 5.7(a) shows that the magnitude of negative velocity observed in the present *d*-type cavity is slightly higher than in the prior studies. Close to the wall the profile obtained in the present study agrees well with prior studies. Away from the wall a reasonable agreement between the present profile and the experimental results of Djenidi et al. (1999) is observed. Slight differences are, however, observed between the values obtained in the present and previous LES of Cui et al. (2003) and experimental studies of Okamoto et al. (1993) results. The pitch-to-height ratio studied in the present and all the prior studies is the same ($p/k = 2$). However, differences in flow blockage and Reynolds number might have led to the slight disparities observed. Fig. 5.7(b) shows that the negative velocity observed in the intermediate cavity of the present study and earlier experimental studies of Okamoto et al. (1993) appears to be the same but is slightly lower compared to the value reported in LES of Cui et al. (2003). For $0.05 < y/h < 0.4$, the streamwise mean velocity observed for the present study over intermediate ribs is slightly lower compared to those reported in LES of Cui et al. (2003) and experimental study of Okamoto et al. (1993). Beyond this range the profiles obtained in the present and prior studies are in good agreement. These disparities can be attributed to the difference in pitch ratios studied in present and the prior studies. From Fig. 5.7(c) it can be observed that for *k*-type cavity the streamwise velocity observed is lower compared to prior studies (Okamoto et al., 1993; Cui et al., 2003) for $y/h < 03$. But a good agreement with prior studies is observed beyond the range mentioned. The differences in the pitch-to-height ratio and

flow blockage might have resulted in the slight disparity between the results close to the wall.

Fig. 5.8 compares the streamwise mean velocity over intermediate and *k*-type rib-tops. For the intermediate rib-top, a reasonably good agreement is observed among the present and prior studies for most part of the profile. But in the range, $0.3 < y/h < 0.65$, the streamwise velocity reported in earlier studies is slightly lower than the present study. Close to the *k*-type ribs, a good agreement between the present profile and the experimental result of Okamoto et al. (1993) is observed. Away from the ribs, however, the velocity profile is slightly higher in the present study than in earlier experimental studies of Okamoto et al. (1993). The present results are in good agreement with LES of Cui et al. (2003) for most part of the profile except very close to the ribs, where the values reported in LES are slightly higher compared to the present study. Again the differences in pitch ratio and Reynolds number for the present and prior studies can be accounted for the slight variations observed in the results.

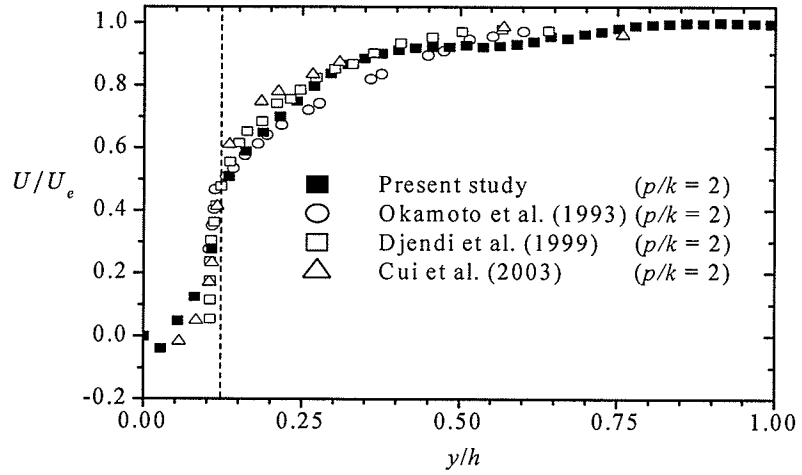

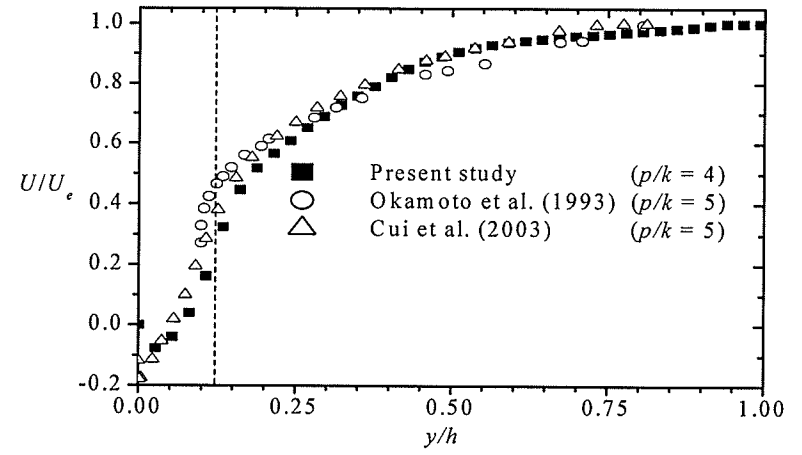

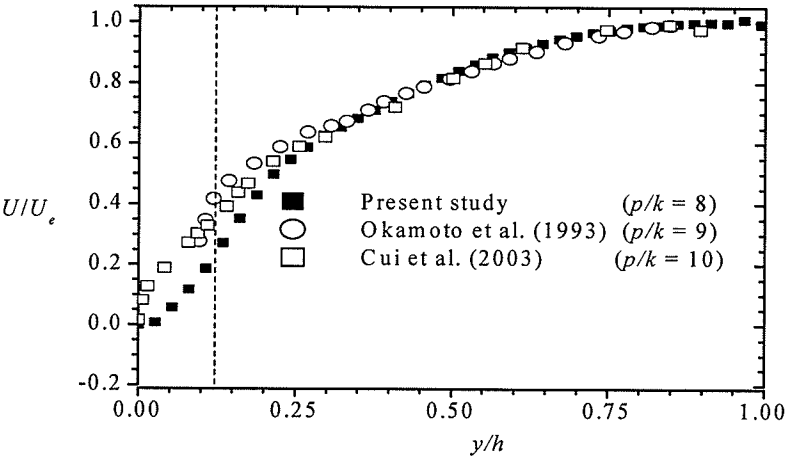

Fig. 5.7 Comparison of streamwise mean velocity in cavity with prior studies (a) *d*-type; (b) intermediate; (c) *k*-type ribs.

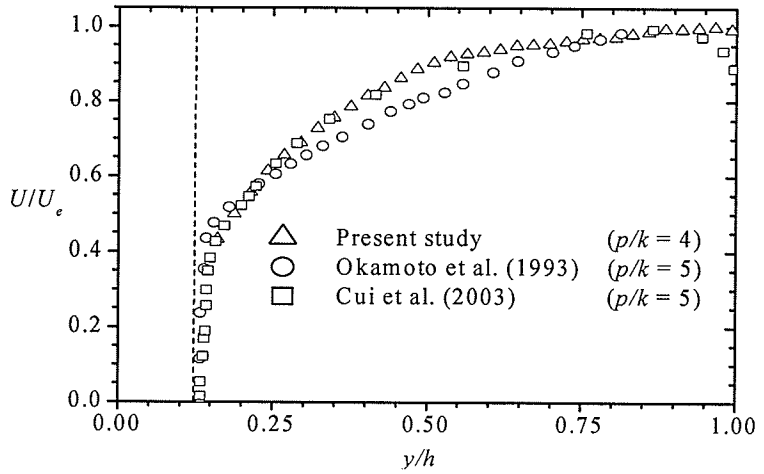

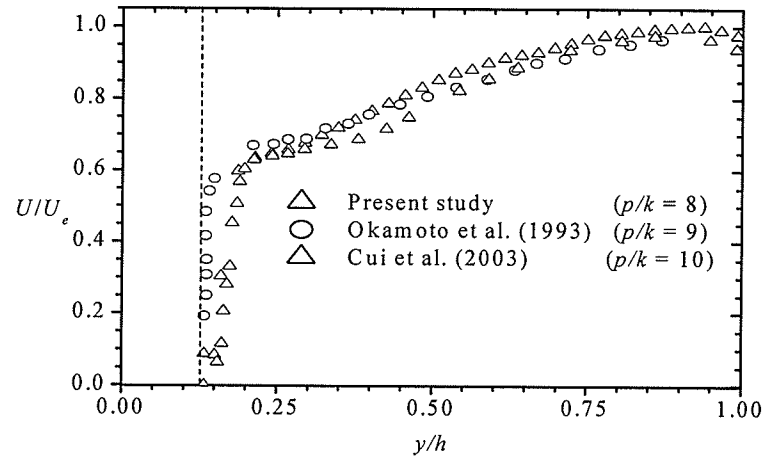

Fig. 5.8 Comparison of mean streamwise velocity over rib-tops with prior studies (a) intermediate; (b) *k*-type ribs.

5.4.2 Turbulent intensity profiles

5.4.2.1 Streamwise turbulent intensity profiles

The profiles of streamwise turbulent intensity, u, normalized by the freestream velocity, U_e, for h = 45 mm and 35 mm are shown in Figs. 5.9 and 5.10, respectively. For the profiles for h = 45 mm, the peak values obtained at the rib-tops of d-type ribs are higher than those obtained in the cavities. All the profiles corresponding to d-type, intermediate and k-type ribs are nearly similar for $y/k > 4$ irrespective of depth of water column, h. Irrespective of depth of water column, the rib-top profiles for d-type, intermediate and k-type ribs vary slightly close to the ribs but collapse onto each other for $y/k > 2$. The peak values obtained for the d-type ribs are not significantly different from the corresponding smooth-wall values. Inside the d-cavity, the profiles at various axial locations are similar for h = 45 mm and h = 35 mm, but the peak values obtained for h = 35 mm profiles are slightly higher than those for h = 45 mm. Slight differences are observed among the various profiles obtained inside the intermediate cavity. However, all these profiles are indistinguishable just above the top plane of the ribs. Because of the stronger interaction between the k-type cavity and the outer flow, the profiles obtained at various axial locations within the cavities for both h = 35 mm and h = 45 mm differ significantly. The differences observed among the various k-type cavity profiles are larger for h = 35 mm compared to those observed for the profiles of h = 45 mm. Figs. 5.9 and 5.10 show that the peak values increase with pitch ratio, p/k. The peak value obtained for k-type ribs for h = 45 mm and h = 35 mm profiles is approximately $(u/U_e)_{max}$ = 0.28. This value is approximately twice as high as the peak value for the smooth-wall and d-type ribs. This observation provides evidence for the effectiveness of k-type ribs to augment turbulence.

The peak value observed for *d*-type cavity in the present study (h = 45 mm) is approximately $(u/U_e)_{max}$ = 0.10. This value agrees well with a value of 0.11 reported in experimental studies of Okamoto et al. (1993) but is lower compared to a value of 0.15 reported in LES of Cui et al. (2003) and LDV study of Djenidi et al. (1999). However, the peak value observed in the cavity of h = 35 mm profile is approximately $(u/U_e)_{max}$ = 0.14, which is in good agreement with the value reported in the earlier LES and LDV studies. The peak value observed in the present study for intermediate (p/k = 4) ribs is approximately $(u/U_e)_{max}$ = 0.16. This value is slightly lower compared to the values of 0.20 and 0.21 in earlier LES and experimental studies, respectively, for their intermediate (p/k = 5) ribs. The peak values obtained in the present study for *k*-type ribs within the cavity and on the rib-top are typically $(u/U_e)_{max}$ = 0.20 and 0.26, respectively. These values observed are in good agreement with the values of 0.20 and 0.25 obtained in prior LES and experimental studies for cavity and rib-top, respectively.

5.4.2.2 Wall-normal turbulent intensity profiles

The profiles of wall-normal turbulent intensity, v, for h = 45 mm and 35 mm are shown in Figs. 5.11 and 5.12, respectively. All the profiles for h = 45 mm and 35 mm over *d*-type, intermediate and *k*-type ribs are qualitatively similar to their corresponding streamwise turbulent intensity profiles. The peak values for the *d*-type ribs are similar to the smooth-wall values. As the pitch-to-height ratio increases, the peak values observed over and between the ribs increase significantly compared to those obtained over the smooth-wall and *d*-type ribs. For *d*-type and *k*-type ribs, the peak values observed for the profiles for h = 35 mm are higher than those observed for h = 45 mm. This disparity can be partly

explained by the increase in the flow blockage for the profiles of $h = 35$ mm compared to the profiles of $h = 45$ mm.

The peak value observed in the d-type cavity for the present profiles ($h = 45$ mm) is approximately $(v/U_e)_{max} = 0.060$. This value is in good agreement with the values of 0.060 and 0.064 in the previous LES and LDV studies, respectively.

(a)

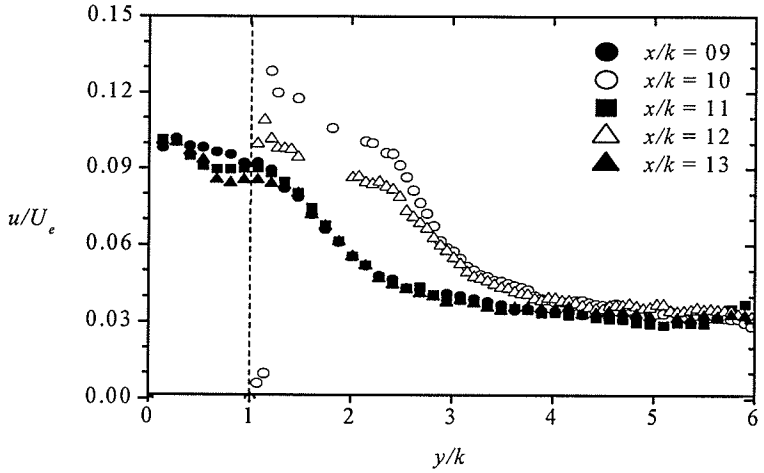

(b)

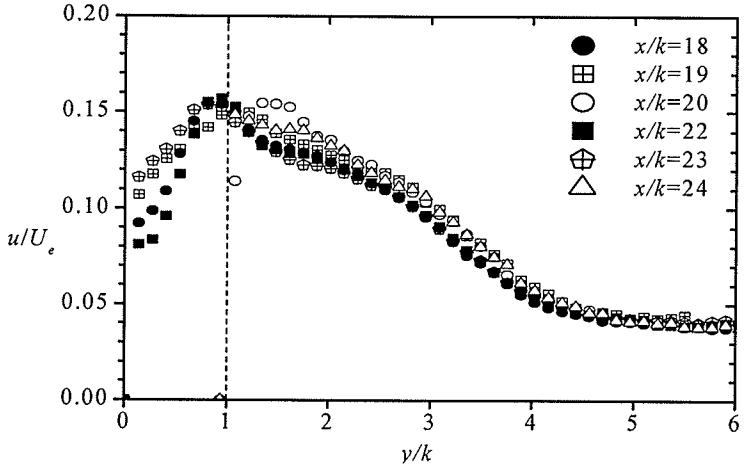

(c)

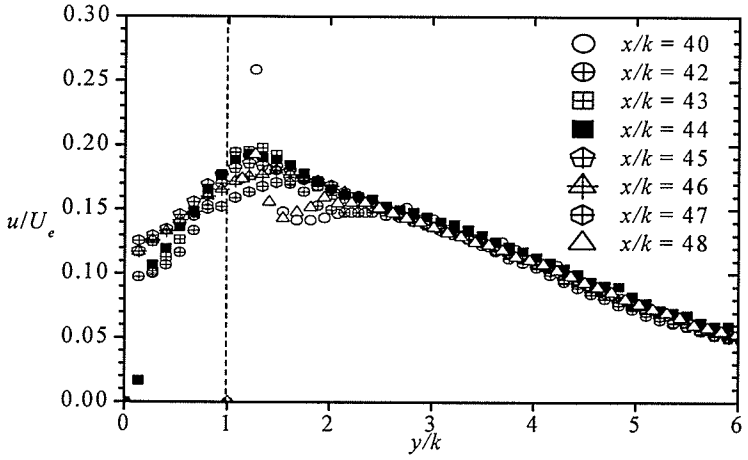

Fig. 5.9 Streamwise turbulent intensity profiles over (a) *d*-type; (b) intermediate; (c) *k*-type ribs for $h = 45$ mm

(a)

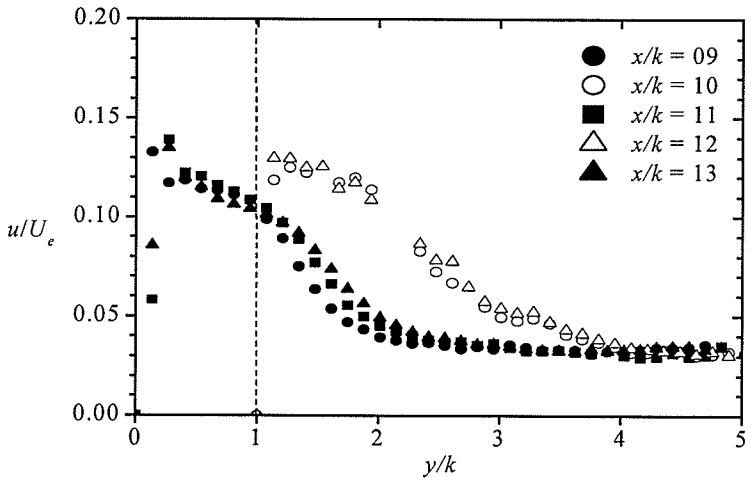

(b)

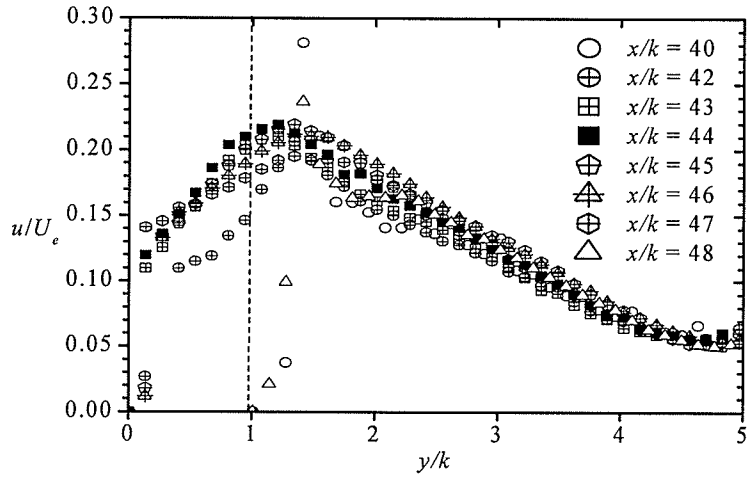

Fig. 5.10 Streamwise turbulent intensity profiles over (a) *d*-type; (b) *k*-type ribs for $h = 35$ mm

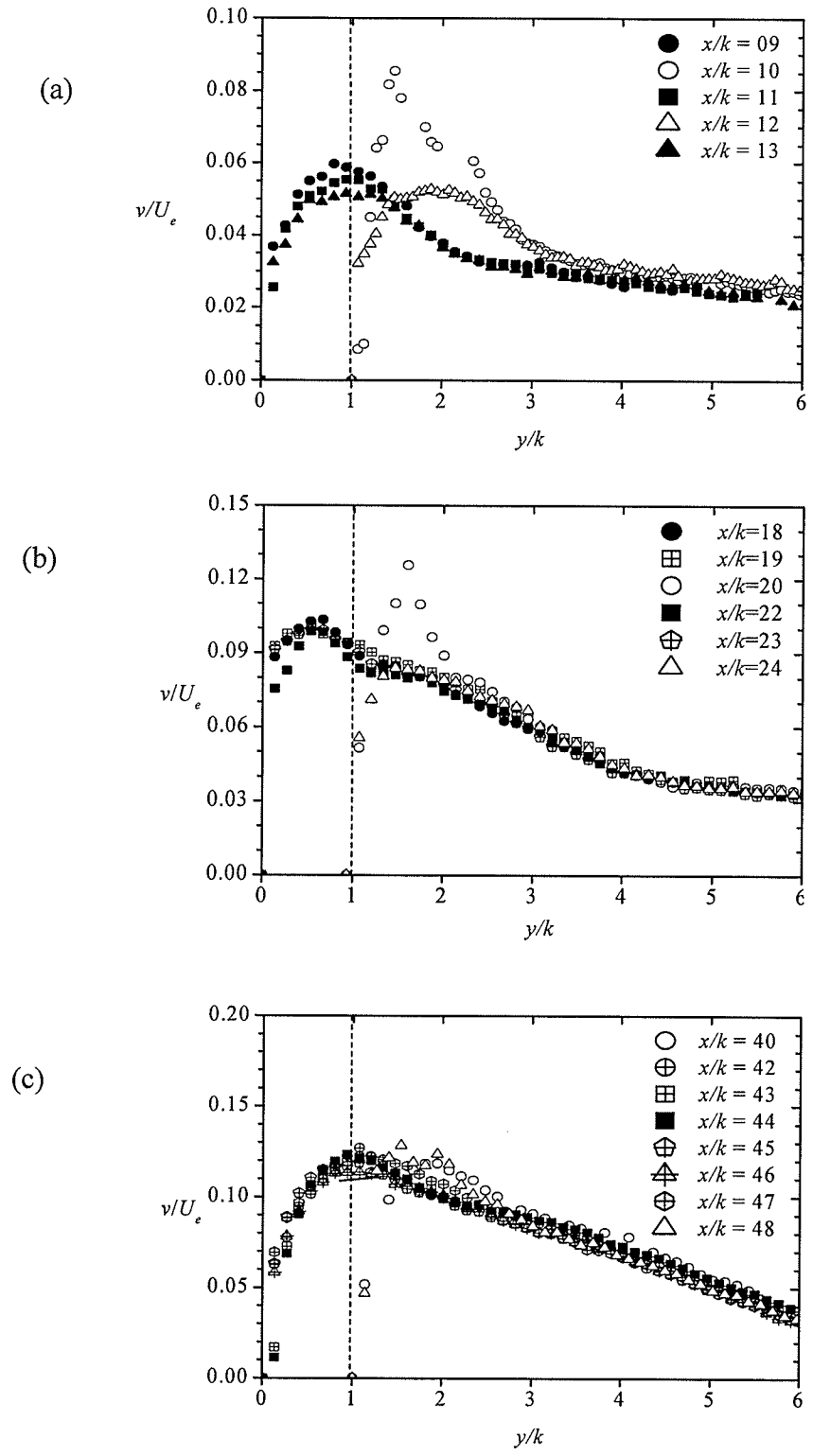

Fig. 5.11 Wall-normal turbulent intensity profiles over (a) *d*-type; (b) intermediate; (c) *k*-type ribs for $h = 45$ mm

(a)

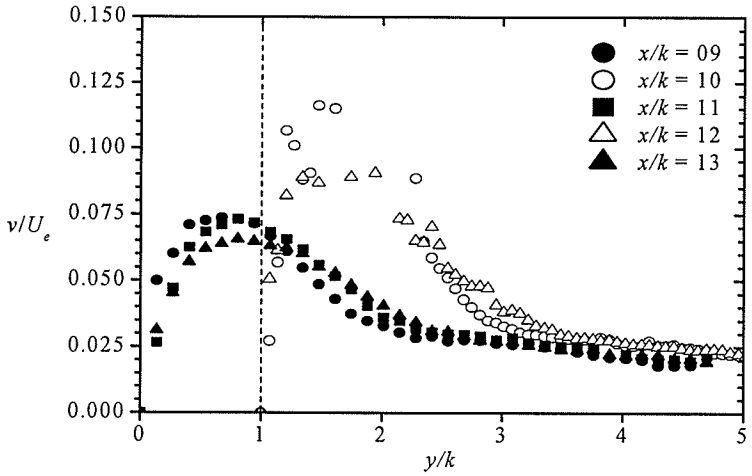

(b)

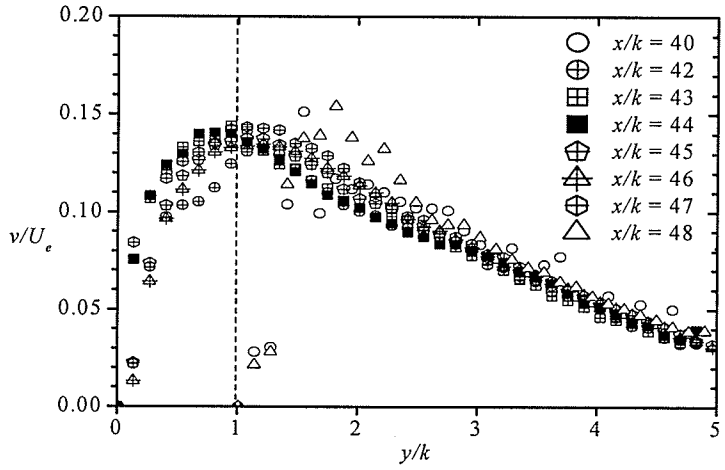

Fig. 5.12 Wall-normal turbulent intensity profiles over (a) *d*-type; (b) *k*-type ribs for $h = 35$ mm

5.4.3 Reynolds shear stress profiles

The Reynolds shear stress profiles for h = 45 mm and 35 mm are shown in Figs. 5.13 and 5.14. All the profiles in this section are normalized by freestream velocity, U_e, and rib height, k. The profiles show higher values close to the wall and decreases smoothly towards the free surface. For the profiles for h = 45 mm, the peak values observed in the cavity of intermediate and k-type ribs are higher than those on the rib-tops. For d-type ribs, however, the peak values observed over the rib-tops are slightly higher than those in the cavities. The profiles for h = 35 mm show higher peak values inside the cavities compared to rib-tops for both d-type and k-type ribs. The various profiles over d-type, intermediate and k-type ribs for both h = 45 mm and h = 35 mm are nearly similar for y/k > 3.5. The profiles corresponding to rib-tops and cavities of d-type ribs collapse on to each other irrespective of depth of water column, h. Incase of the intermediate rib, the rib-tops (x/k = 20, 24) are indistinguishable right from the rib-top, but the various profiles inside the cavity differ slightly. However, these profiles collapse onto each other slightly above the top plane of the ribs. As noted earlier for the k-type ribs, the profiles inside the cavity differ significantly for h = 35 mm, however, the differences are smaller for h = 45 mm profiles. The peak values of the Reynolds shear stress increase with p/k. Furthermore the peak values obtained over and between the ribs are significantly higher than those obtained over the upstream smooth-wall. Similar to the turbulent intensity, the peak values observed for Reynolds shear stress for h = 35 mm profiles shows slightly higher values than those of h = 45 mm profiles.

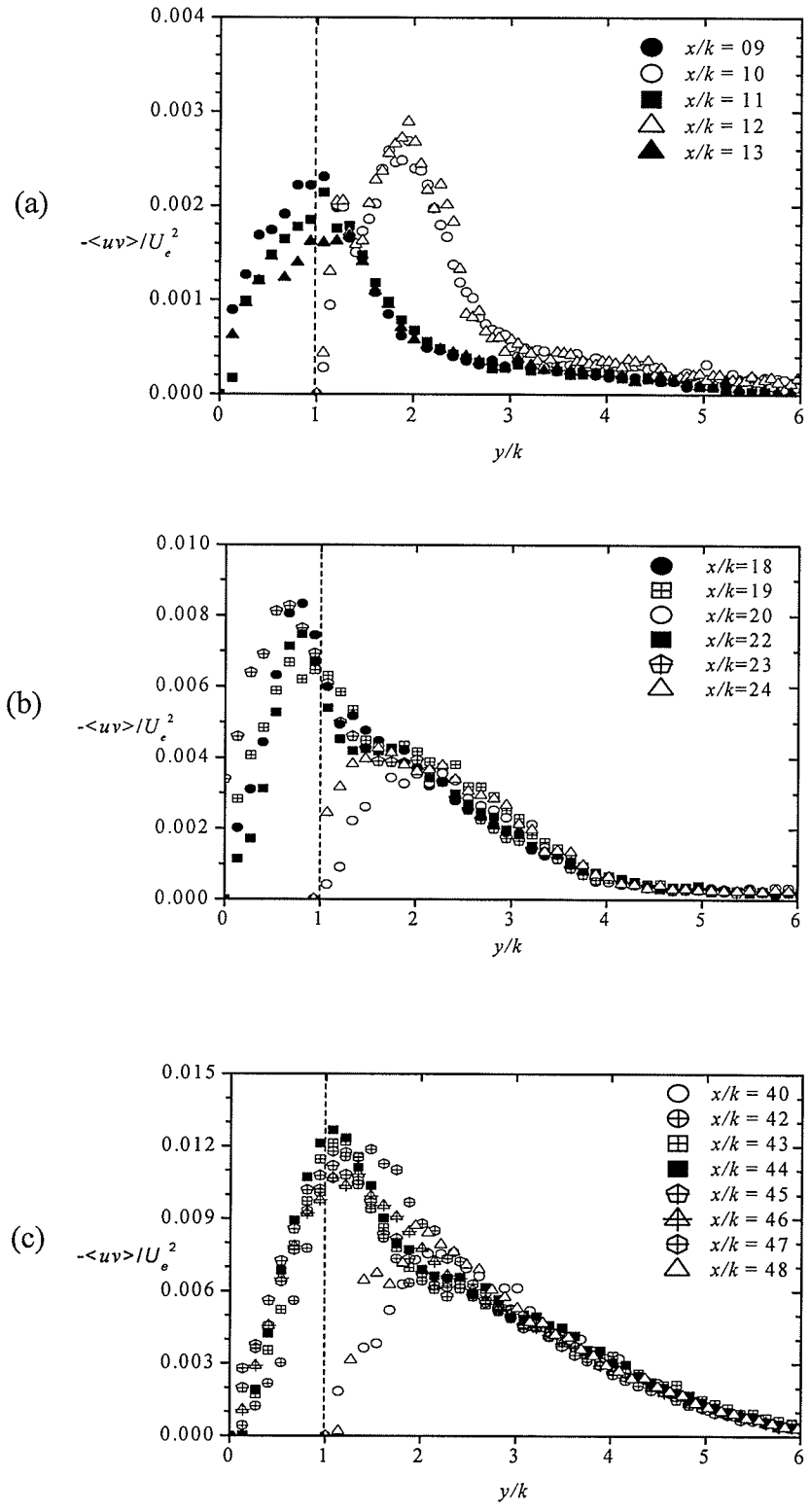

Fig. 5.13 Reynolds shear stress profiles over (a) *d*-type; (b) intermediate; (c) *k*-type ribs for $h = 45$ mm

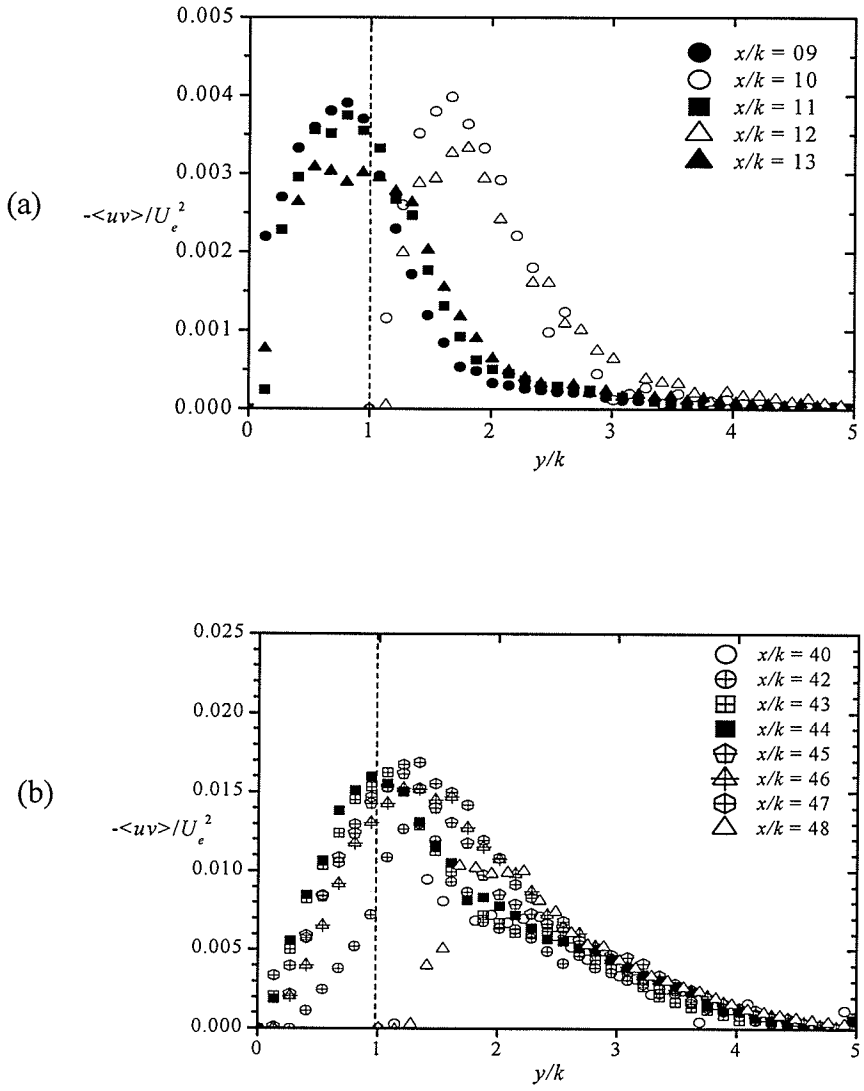

Fig. 5.14 Reynolds shear stress profiles over (a) *d*-type; (b) *k*-type ribs for $h = 35$ mm

5.5 Spatial averaged profiles

Because of the significant variation of the mean and turbulent quantities in the cavity and above the crests of the ribs (for *k*-type), it was decided to average the mean and turbulent quantities over a pitch *p*, from one rib-top to other, and compare the profiles of different *p/k*. For each rib type, the mean velocity and turbulent quantities at various locations between ribs 6 and 7 were averaged. The following mathematical relationship is used for calculating the spatial averaged mean streamwise velocity:

$$U(y) = p/2.5 \int_{x'=0}^{x'=p} U(y)\, dx' \qquad [5.1]$$

$x' = 0$, $x' = p$ corresponds to the centers of ribs 6 and 7, respectively, and, U, is the streamwise mean velocity. Eqn. 5.1 was also used to calculate the spatial averaged turbulent quantities by replacing the streamwise velocity in Eqn. 5.1 with the turbulent quantities.

5.5.1 Mean velocity and turbulent quantities in outer co-ordinates

The spatial averaged profiles for the *d*-type, intermediate and *k*-type ribs for $h = 45$ mm are presented in this section. As mentioned earlier the profiles presented in this section correspond to the average between ribs 6 and 7 for *d*-type, intermediate and *k*-type ribs. For *d*-type and intermediate ribs an additional profile corresponding to the average between the ribs 5 and 6 is also included. All the profiles in this section are normalized in outer co-ordinates (U_e, k).

Fig. 5.15 shows the mean streamwise velocity profiles. For *d*-type ribs, the profiles show slight variation up to $y/k \leq 2.5$ but are indistinguishable beyond this range.

However, for intermediate ribs the profiles corresponding to average between ribs 5-6 and 6-7 collapsed on to each other for the entire depth of water column. Fig. 5.16 show the distribution of the streamwise turbulent intensity. All the profiles show a peak close to rib height and falls off smoothly towards the free surface. The peak value of the streamwise turbulent intensity for *d*-type ribs is approximately $(u/U_e)_{max} = 0.125$, which is similar to the peak value obtained for smooth-wall. However, the peak value observed for *k*-type ribs is approximately 1.6 times as high as the value obtained for the smooth-wall and *d*-type ribs. Fig. 5.17 shows the comparison of the wall-normal turbulent intensity profiles. The various profiles over the *d*-type and intermediate ribs collapse on to each other very well. The trend observed for every profile is similar to that observed for the streamwise turbulent intensity profile except that the wall-normal turbulent intensity values are comparatively lower. Reynolds shear stress profiles are shown in Fig. 5.18. The profiles corresponding to the average between ribs 5-6, and ribs 6-7 for *d*-type as well as intermediate ribs collapse onto each other. The figure shows that the level of Reynolds shear stress increases with increasing *p/k*. The peak Reynolds shear stress value observed for the *k*-type and intermediate ribs are $(-\langle uv \rangle / U_e^2)_{max} = 0.0125$ and 0.006, respectively. These values for *k*-type and intermediate ribs are approximately 5 times and 2.4 times as high as the peak value of 0.0025 observed for *d*-type ribs.

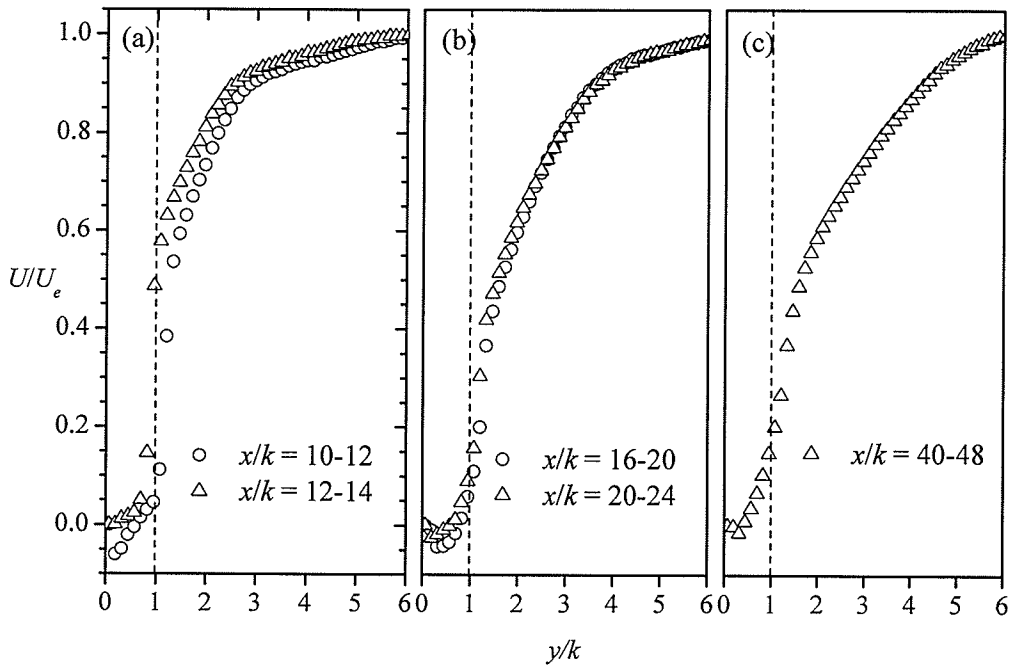

Fig. 5.15 Spatial averaged mean streamwise velocity profiles over (a) *d*-type; (b) intermediate; (c) *k*-type ribs.

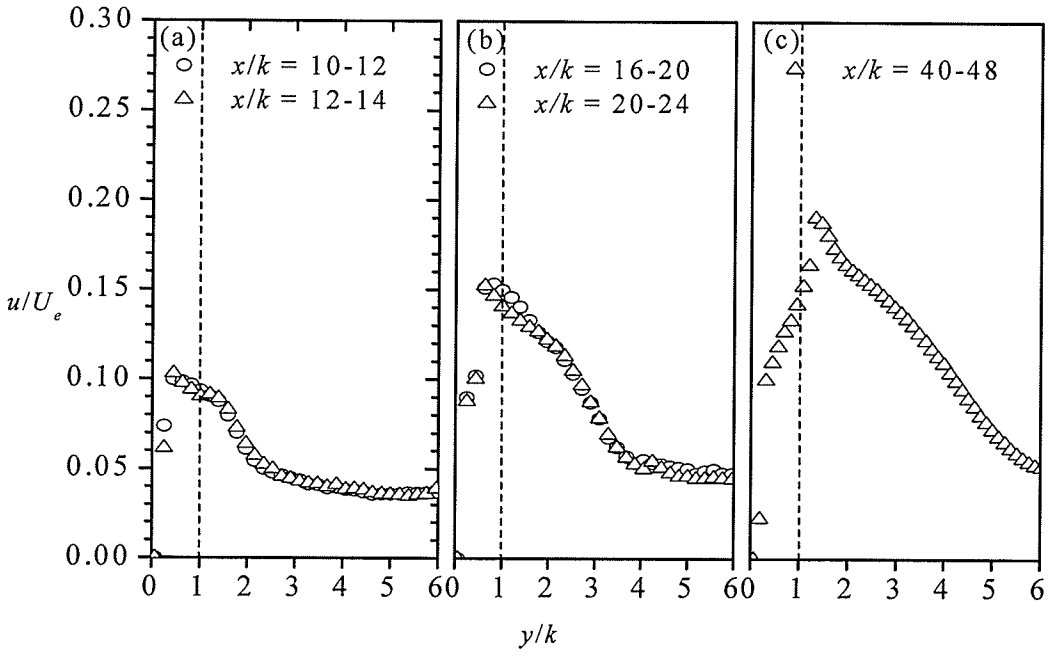

Fig. 5.16 Spatial averaged streamwise turbulent intensity profiles over (a) *d*-type; (b) intermediate; (c) *k*-type ribs.

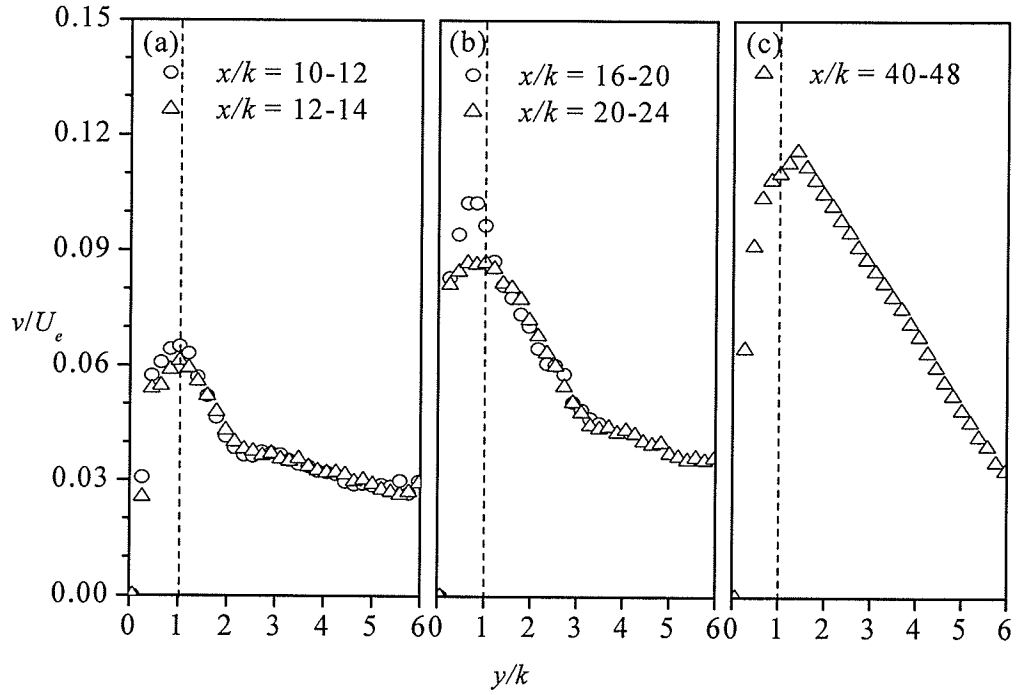

Fig. 5.17 Spatial averaged wall-normal turbulent intensity profiles over (a) *d*-type; (b) intermediate; (c) *k*-type ribs.

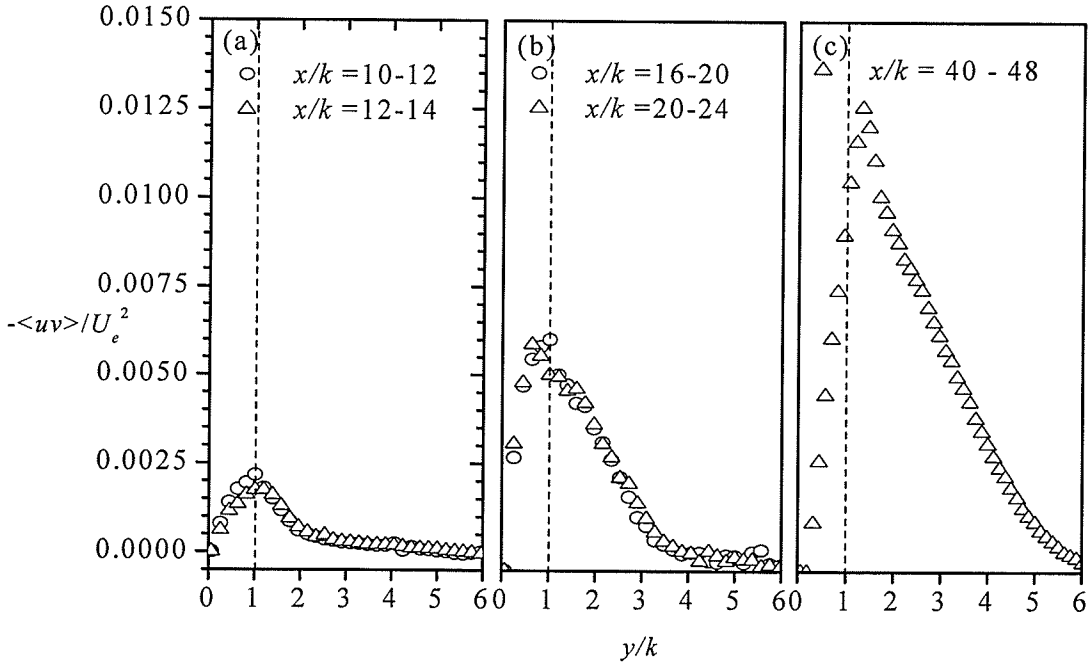

Fig. 5.18 Spatial averaged Reynolds shear stress profiles over (a) *d*-type; (b) intermediate; (c) *k*-type ribs.

5.5.2 Mean velocity profiles in inner co-ordinates

As previously mentioned, one effect of surface roughness on the mean flow is to increase the skin friction coefficient, $C_f = 2(U_\tau/U_e^2)$. The friction velocities for both the smooth and the various rib types were obtained using the Clauser chart technique, that is, fitting the mean velocity profiles to classical log-law: $U^+ = \kappa^{-1} \ln(y^+) + B - \Delta U^+$. The following values were adopted for the log-law constants: $\kappa = 0.41$ and $B = 5.0$. The uncertainty in U_τ is estimated to be of order 5% and 10% for the smooth wall and ribs, respectively.

Fig. 5.19(a) and 5.19(b) shows the averaged streamwise mean velocity profiles plotted in inner co-ordinates in a semi logarithmic format for h = 45 mm and 35 mm, respectively. For the smooth-wall profile, the data and log-law overlap up to $y^+ \approx 500$ because of the small wake component compared to a classical zero pressure gradient turbulent boundary layer. Agreement between data and the log-law with the appropriate roughness function is good up to $y^+ \approx 300$, 700 and 800 for *d*-type, intermediate and *k*-type roughness, respectively for h = 45 mm. Similar trends were observed for h = 35 mm profiles. The values of U_τ and ΔU^+ for the averaged velocity profiles are summarized in Table 5.1. Figs. 5.19(a), 5.19(b) and Table 5.1 clearly show that the roughness shift ΔU^+ is smallest for *d*-type roughness and largest for *k*-type roughness. The skin friction values are higher for the ribs than for the upstream smooth-wall profile because of contribution from the pressure-induced drag. It is seen that the pressure-induced drag (and hence C_f value) increases with pitch-to-height ratio, as predicted.

5.5.3 Drag characteristics of rib-roughness

In the present study the values of k_s were calculated from the relation, $\Delta U^+ = \kappa^{-1} \ln(k_s^+) + B - C$ where $C = 8.5$. The dimensionless sand grain roughness number, $k_s^+ = k_s U_\tau / \upsilon$, and k_s/k values are summarized in Table 5.1. It is observed that the values of k_s^+ and k_s/k vary significantly with the rib configuration. In general, k_s^+ and k_s/k values are highest for k-type ribs and least for d-type ribs. For the present intermediate ribs ($p/k = 4$) the value of $k_s/k = 4.34$. This value is higher than $k_s/k = 3.20$ obtained from LES ($p/k = 5$) in a channel roughened with square ribs but lower than $k_s/k = 6.06$ obtained in measurements over circular ribs in a zero pressure gradient turbulent boundary layer (Krogstad and Antonia, 1999, $p/k = 4$). The disparity might be because of uncertainties in U_τ and differences in the Reynolds numbers used in the studies. For the present k-type ribs ($p/k = 8$), $k_s/k = 6.79$ which is higher than $k_s/k = 5.90$ obtained in the LES of Cui et al. (2003) in channel roughened by square ribs ($p/k = 9$). The rough-wall parameters obtained for $h = 35$ mm are similar to those obtained for $h = 45$ mm in many cases. However, the values of ΔU^+ and k_s/k for k-type ribs are lower for $h = 35$ mm than for $h = 45$ mm. The disparity may be due to the increase in flow blockage, which would have caused local acceleration of the flow. The ratio k_s/k provides insight into the effectiveness of transverse square ribs to augment flow resistance compared to mono-disperse sand grains. For example, 40 mm diameter of mono-disperse sand grains covering the entire bottom wall of the channel will be required to produce the same flow resistance observed for the present k-type while only 2.2 mm diameter sand grains are necessary to produce the resistance observed over d-type ribs.

Table 5.2 shows the values of U_τ/U_e and ΔU^+ obtained in the present study and DNS results in channel roughened on one side with circular and square two dimensional ribs (Leonardi et al., 2003, 2004, 2005), LES of Cui et al. (2003), and measurements in a zero pressure gradient turbulent boundary layer over circular ribs (Krogstad and Antonia, 1999). Table 5.2 reveals that the roughness function ΔU^+ and U_τ/U_e increase with pitch ratio (*p/k*). This means that the drag characteristics also increase with *p/k*. For *d*-type ribs, the major portion of the total drag (friction drag + pressure drag) is contributed by friction. For intermediate and *k*-type ribs, on the other hand, the pressure drag contributes more towards the total drag. Therefore, the drag characteristics of *d*-type ribs are more sensitive to changes in flow Reynolds number than the intermediate and *k*-type ribs. From Table 5.2, it can be observed that the values of U_τ/U_e for *d*-type and *k*-type ribs are similar for both h = 45 mm and h = 35 mm data. The values of ΔU^+ in the present study (h = 45 mm and h = 35 mm) are also similar for *d*-type ribs but value for *k*-type ribs for h = 35 mm is slightly lower than for h = 45 mm. This disparity could be attributed to uncertainties in measurements of U_τ and possible blockage effects.

Consideration is now turned to comparison with prior studies. For the *d*-type ribs, values of U_τ/U_e obtained in the present study (0.08 for h = 45 mm and h = 35 mm) are approximately 33% and 60% higher than the values reported in DNS for round ribs and square ribs, respectively. The values obtained for the intermediate and *k*-type ribs in the present study, are approximately 55% and 37% higher than the values reported in the DNS study over round and square ribs, respectively. In the boundary layer study (Krogstad and Antonia, 1999), U_τ/U_e = 0.06 which is approximately 45% of the value obtained in the present study for the same pitch ratio. The disparity observed decreases

from *d*-type to *k*-type roughness, and this can not be completely attributed to measurement uncertainties. The Reynolds number based on roughness height, k and freestream velocity, U_e used in present study, DNS, LES and in boundary layer flows are 1560, 840, 1000 and 11200, respectively. Similarly, the blockages in present study, DNS, LES and in boundary layer flows are 13%, 20%, 10% and 2%, respectively. The differences in flow Reynolds number and blockage may partly explain the differences observed above. Compared to the LES results, the values of ΔU^+ obtained in the present study are about 55% higher for p/k = 2, and 4% and 7% lower for intermediate and *k*-type, respectively. Compared to present study the values reported in DNS are 53%, 24% and 5% lower for p/k = 2, 4 and 8 respectively.

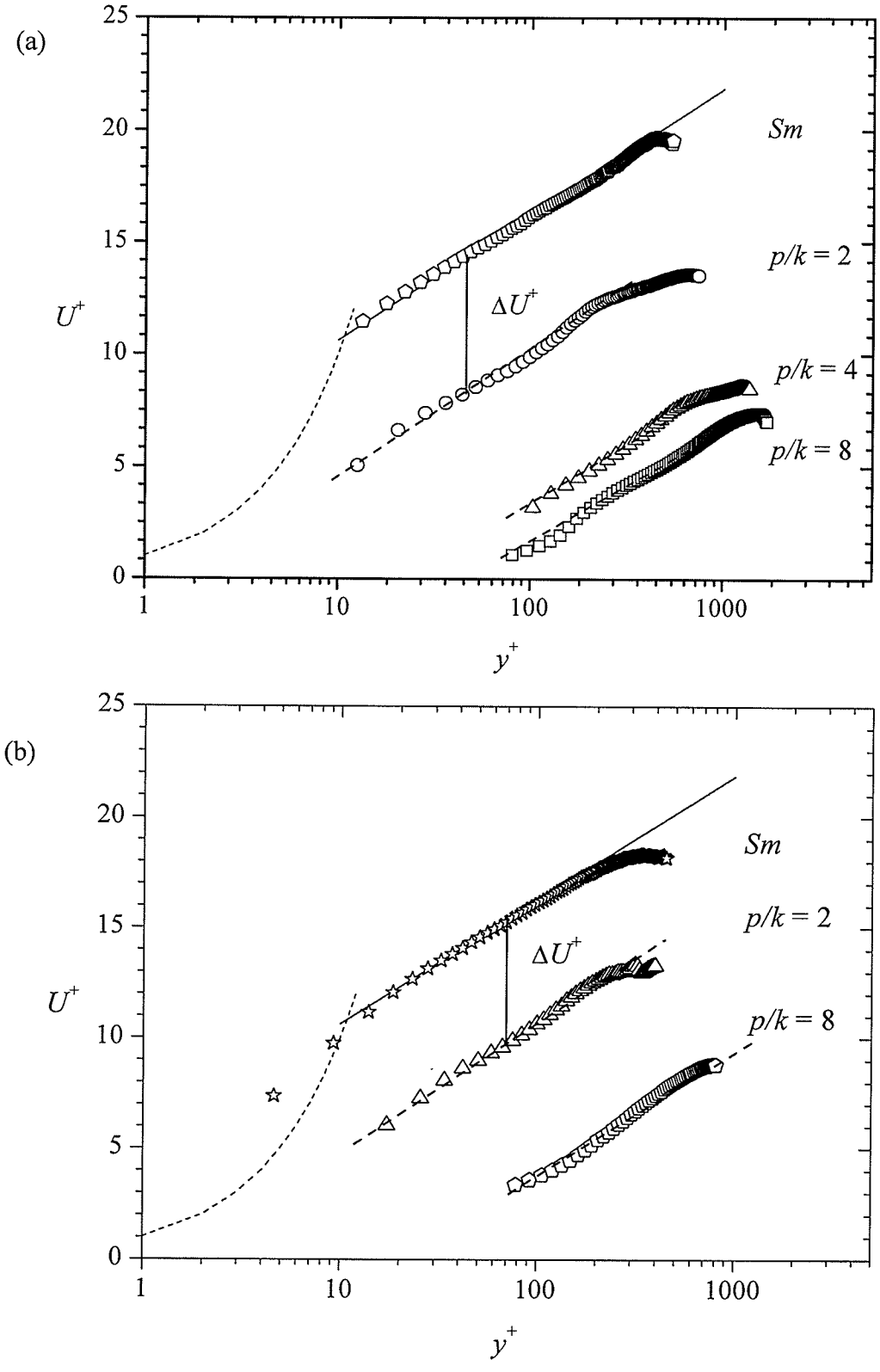

Fig. 5.19 Mean velocity profiles in inner co-ordinates: (a) $h = 45$ mm; (b) $h = 35$ mm.

h mm	*Surface type*	U_e m/s	U_τ m/s	U_τ/U_e	C_f $\times 10^{-3}$	ΔU^+	δ mm	θ mm	k_s^+	k_s/k
45	*SM*	0.21	0.010	0.050	5.50	---	36.6	3.72	---	---
	$p/k = 2$	0.26	0.019	0.073	11.00	5.6	36.6	3.75	42	0.37
	$p/k = 4$	0.26	0.031	0.119	26.45	12.6	38.2	4.12	808	4.34
	$p/k = 8$	0.29	0.035	0.120	28.80	13.9	38.2	4.92	1590	6.79
35	*SM*	0.21	0.011	0.052	5.83	---	22.9	2.14	---	---
	$p/k = 2$	0.26	0.020	0.080	12.00	5.6	31.4	2.17	42	0.60
	$p/k = 8$	0.29	0.035	0.120	28.80	13.0	31.4	3.77	867	4.15

Table 5.1 Smooth and rough-wall parameters

Roughness type	***d*-type**		**intermediate**		***k*-type**	
Quantity measured	U_τ/U_e	ΔU^+	U_τ/U_e	ΔU^+	U_τ/U_e	ΔU^+
Present study, $h = 45$ mm (Square ribs)	0.073	5.6	0.119	12.6	0.120	13.9
Present study, $h = 35$ mm (Square ribs)	0.080	5.6	--	--	0.120	13.0
Leonardi et al., 2005 (Square ribs)	0.048	2.6	0.074	9.5	0.088	13.2
Leonardi et al., 2005 (Round ribs)	0.058	--	0.074	--	0.088	--
Cui et al., 2003 (Square ribs)	--	3.6	--	13.2	--	15.0
Krogstad et al., 1999 (Round ribs)	--	--	0.057	10.5		

Table 5.2 Comparison of drag parameters

d-type roughness: $p/k = 2$ in the present and previous studies; intermediate roughness: $p/k = 4, 4, 4, 5$ for present, Leonardi et al. (2005), Krogstad et al. (1999) and Cui et al. (2003) studies, respectively; *k*-type roughness: $p/k = 8, 8, 10$ for present, Leonardi et al. (2005), and Cui et al. (2003) studies, respectively.

CHAPTER 6

SUMMARY AND CONCLUSIONS

6.1 Summary

In this thesis, a particle image velocimetry technique was used to study open-channel turbulent flow over two-dimensional transverse square ribs. The rib height was kept constant but the pitch between adjacent ribs was varied to produce the so-called *d*-type, intermediate and *k*-type ribs. Two depths of water column were studied. The mean velocity vectors, streamlines, vorticity contours, and profiles of the mean velocity, turbulent intensities and Reynolds shear stress were used to document the similarities and differences between the present study and previous studies of zero pressure gradient turbulent boundary layers and fully developed channel flows over transverse ribs.

The velocity vectors and streamlines over and between the different rib types show that the *d*-type and intermediate cavities are completely occupied by stable clockwise rotating vortices. These vortices prevented the outer flow from reattaching onto the cavity floor. As a result, turbulent flows over *d*-type and intermediate ribs remain largely unaffected above the top plane of the ribs. For the *k*-type ribs on the other hand, the outer flow reattached onto the floor of the cavity. A stronger interaction between the *k*-type cavities and outer flow was observed. This interaction enhances momentum transport between the outer flow and the *k*-type cavities compared to the cavities of the *d*-type and intermediate ribs.

The results show that one effect of rib-roughness on the mean flow is to augment the drag characteristics compared to the smooth-wall. The drag characteristics were observed to increase dramatically as the pitch-to-height ratio increases. The turbulence levels over the *d*-type ribs were nearly the same as over the

smooth-wall. This indicates that *d*-type ribs are not effective in augmenting turbulence. The turbulence intensities and Reynolds shear stress were observed to increase substantially as the as the pitch-to-height ratio increases. There were no or only slight differences between the profiles obtained for the two water depths. These differences may be attributed to the difference in the flow blockage.

The present results agreed reasonably well with previous numerical and experimental studies conducted in boundary layers and fully developed channels. For example, the downward shift in the mean velocity profiles is similar to the values reported in prior LES results of Cui et al. (2003). Similar agreements were observed between the profiles of turbulent intensities and Reynolds shear stress obtained in the present and the previous studies.

6.2 Conclusions

The following specific conclusions are drawn from the experimental results presented in the chapter 5.

- The interaction between the outer flow and the shear layers generated by the ribs is strongest for *k*-type and least for *d*-type ribs.
- The levels of turbulent quantities increase with increasing pitch-to-height ratio.
- The roughness shift, skin friction coefficient and other drag characteristics increase substantially with increasing pitch-to-height ratio.
- The present results show a reasonable agreement with the previous experimental and numerical studies over transverse ribs conducted in fully developed channel and boundary layers.

6.3 Future work

The present study considered open-channel turbulent flows over and between transverse square ribs for three pitch-to-height ratios. Though this study provides insight into the variation of mean velocity and turbulent quantities inside and above the crest of the ribs, it will be useful to conduct simultaneous velocity and concentration measurements for different pitch-to-height ratios. The study of pressure gradient turbulent flows over transverse ribs will be useful in understanding the combined effects of pressure gradient and rib-roughness on near-wall turbulence structure.

REFERENCES

[1] Acharya, M., Bornstein, J., and Escudier, M. P., 1985, "Turbulent boundary layers on rough surfaces," Fifth symposium on turbulent shear flows, Ithaca, New York, USA, pp. 2.7-2.12.

[2] Adrian, R. J., 1991, "Particle imaging techniques for experimental fluid mechanics," Annual Review of Fluid Mechanics, Vol. 23, pp. 261-304.

[3] Akinlade, O. J., Bergstrom, D. J., Tachie, M. F., and Castillo, L., 2004, "Outer flow scaling of smooth and rough-wall turbulent boundary layers," Experiments in Fluids, Vol. 37, pp. 604-612.

[4] Alireza, A., Anderson, I. H., and Manhart, M., 2004, "DNS of turbulent flow in a rod-roughened channel," International Journal of Heat and Fluid Flow, Vol. 25, pp. 373-383.

[5] Antonia, R. A., 2001, "Turbulence structure over different types of surface roughness," Fluid Dynamics Research, Vol. 28, pp. 139-157.

[6] Balachandar, R., and Blakely, D., 2004, "Surface roughness effects on turbulent boundary layers on a flat plate located in an open-channel," Journal of Hydraulic Research, Vol. 42, pp. 247-261.

[7] Bergstrom, D. J., Kotey, A. N., and Tachie, M. F., 2002, "The effects of surface roughness on the mean velocity profile in a turbulent boundary layer," ASME Journal of Fluids Engineering, Vol. 124, pp.1-7.

[8] Bergstrom, D. J., Akinlade, O. J., and Tachie, M. F., 2004, "Skin friction correlation for smooth-wall and rough-wall turbulent boundary layers," Journal of Fluids Engineering, Transactions of the ASME, Vol. 127, pp. 1146-1153.

[9] Clauser, F. H., 1954, "Turbulent boundary layers in adverse pressure gradients," Journal of the Aeronautical sciences, Vol. 21, pp. 91-108.

[10] Coles, D. E., 1956, "The law of the wake in the turbulent boundary layer," Journal of Fluid Mechanics, Vol. 1, pp. 191-226.

[11] Coleman, W. H., and Steele W.G., 1999, "Experimental and uncertainty analysis for Engineers," Second Edition, John Wiley & Sons. Inc., New York

[12] Cui, J., Patel, C. V., and Lin C. L., 2003, "Large eddy simulation of turbulent flow in a channel with rib-roughness," International Journal of Heat and Fluid Flow, Vol. 24, pp. 372-388.

[13] Djenidi, L., Elavarasan, R., and Antonia, R. A., 1999, "The turbulent boundary layer over transverse square cavities," Journal of Fluid Mechanics, Vol. 395, pp. 271-294.

[14] Grant, I., 1997, "Particle image velocimetry: a review," Proceedings of Institution of Mechanical Engineers, Vol. 211, pp. 55-76.

[15] Hama, F. B., 1954, "Boundary layer characteristics for smooth and rough surfaces," Shipbuilder and Marine Engine Builder, Vol. 62, pp. 266-270.

[16] Islam, S. M., Haga, K., Kaminaga, M., Hino, R., and Monde, M., 2004, "Experimental analysis of turbulent flow structure in a fully developed rib-roughened rectangular channel with PIV," Experiments in Fluids, Vol. 33, pp. 296-306.

[17] Jimenez, J., 2004, "Turbulent flows over rough-walls," Annual Review of Fluid Mechanics, Vol. 36, pp.173-196.

[18] Keane, R. D., and Adrian, R. J., 1990, "Optimization of particle image velocimeters, Part 1: Double pulsed systems," Measurement Science and Technology, Vol. 1, pp. 1202-1215.

[19] Keane, R. D., and Adrian, R. J., 1992, "Theory of cross-correlation analysis of PIV images," Applied Scientific Research, Vol. 49, pp.191-215.

[20] Krogstad, P.A., and Antonia, R.A., 1999, "Surface roughness effects in turbulent boundary layers," Experiments in Fluids, Vol. 27, pp. 450-460

[21] Krogstad, A. P., Anderson, I. H., Bakken, M. O., and Ashrafian, A., 2005, "An experimental and numerical study of channel flow with rough-walls," Journal of Fluid Mechanics, Vol. 530, pp. 327-352.

[22] Leonardi, S., Orlandi, P., Smalley, R. J., Djenidi, L., and Antonia, R. A., 2003, "Direct numerical simulations of turbulent channel flow with transverse square bars on one wall," Journal of Fluid Mechanics, Vol.491, pp. 229-238.

[23] Leonardi, S., Orlandi, P., Djenidi, L., and Antonia, R. A., 2004, "Structure of turbulent channel flow with square bars on one wall," International Journal of Fluid Flow, Vol. 25, pp. 384-392.

[24] Leonardi, S., Orlandi, P., and Antonia, R. A., 2005, "A method for determining the frictional velocity in a turbulent channel flow with roughness on bottom wall," Experiments in Fluids, Vol. 38, pp. 796-800.

[25] Ligrani, P. M., and Moffat, R. J., 1986, "Structure of transitionally rough and fully rough turbulent boundary layers," Journal of Fluid Mechanics, Vol. 162, pp. 69-98.

[26] Liou, M. T., and Kao, F. C., 1988, "Symmetric and Asymmetric turbulent flows in a rectangular duct with a pair of ribs," Journal of Fluids Engineering, Vol. 110, pp. 373-379.

[27] Mei, R., Adrian, R. J., and Hanratty, T. J., 1991, "Particle dispersion in isotropic turbulence under strokes drag and basset force with gravitational settling," Journal of Fluid Mechanics, Vol. 225, pp. 481-495.

[28] Meng, N., Pletcher, R. H., and Simons, T. A., 1999, "Large eddy simulation of a turbulent channel flow with a rib-roughened wall," AIAA Aerospace Sciences, 37th Meeting and Exhibit, pp. 1-8.

[29] Millikan, C. B., 1938, "A critical discussion of turbulent flows in channels and circular tubes," Proceeding of 5th International Congress of Applied Mechanics, Cambridge, pp. 386-392.

[30] Mullin, T., and Martin, R. S., 1991, "Intermittent phenomena in the flow over a rib-roughened surface," Transactions of ASME, Vol. 113, pp. 206-209.

[31] Nagano, Y., Hattori, H., and Houra, T., 2004, "DNS of velocity and thermal fields in turbulent channel flow with transverse-rib roughness," International Journal of Heat and Fluid Flow, Vol. 25, pp. 393-403.

[32] Nikuradse, J., 1933, "Stromungsgesetz in rauhren rohren," VDI-Forschungsheft, 361 (English Translation, 1950, "Laws of flow in rough pipes," Technical Report, NACA Technical Memo, 1292, National Advisory Commission For Aeronautics, Washington, DC).

[33] Okamoto, S., Seo, S., Nakaso, K., and Kawai, I., 1993, "Turbulent shear flow and heat transfer over the repeated two-dimensional square ribs on ground plane," Journal of Fluids Engineering, Vol. 115, pp. 631-637.

[34] Perry, A. E., Schofield, W. H., and Joubert, P. N., 1969, "Rough-wall turbulent boundary layers," Journal of Fluid Mechanics, Vol. 37, pp. 383-413.

[35] Raffel, M. M., Gharib, O., Ronneberger, J., and Kompenhans, J., 1995, "Feasibility study of three-dimensional PIV by correlating images of particles within parallel light sheet planes," Experiments in Fluids, Vol. 19, pp. 69-77.

[36] Raupach, M. R., Antonia, R. A., and Rajagopalan, S., 1991, "Rough-wall turbulent boundary layers," Applied Mechanics Review, Vol. 44, pp. 1-25.

[37] Sato, H., Hishida, K., and Maeda, M., 1989, "Turbulent flow characteristics in a rectangular channel with repeated rib-roughness," National Heat transfer Conference, Vol. 107, pp. 191-196.

[38] Schlichting, H., 1936, "Experimentelle untersuchungen zum Rauhigkeits problem," Ingenieur Archiv, Vol. 7, pp. 1-34 (English translation, 1937, "Experimental investigation of the problem of surface roughness," NACA Technical Memo, 823, Vol. 7, pp. 191-196).

[39] Schlichting, H., 1979, "Boundary layer theory," McGraw Hill Book Company, New York.

[40] Sleath, F. A., 1988, "Transition in oscillatory flow over rough beds," Journal of Waterway, Port, Costal and Ocean Engineering, Vol. 114, pp. 18-33.

[41] Spooren, R., Dyrseth, A. A., and Vaz, M., 1994, "Electronic shear interferometry application of a (double-) pulsed laser," Applied Optics, Vol. 32, pp. 4719-4727.

[42] Tani, J., 1987, "Turbulent boundary layer development over rough surfaces," In: Perspectives in turbulence studies, Editors Meier H. U and Bradshaw P, Berlin, Springer-Verlag, pp. 223-249.

[43] Tachie, M. F., Bergstrom, D. J., and Balachandar, R., 2003, "Roughness effects in low Re_θ open-channel turbulent boundary layers," Experiments in Fluids, Vol. 35, pp. 338-346.

[44] Westerweel, J., 1993, "Digital particle image velocimetry-theory and application," PhD thesis, Delft University Press, Delft, Netherlands.

[45] Westerweel, J., 1994, "Efficient detection of spurious vectors in particle image velocimetry data," Experiments in Fluids, Vol. 16, pp. 236-247.

[46] Westerweel, J., Draad, A. A., van der Hoeven, J. G., and Van, O. J., 1996, "Measurement of fully developed turbulent pipe flow with digital PIV," Experiments in Fluids, Vol. 20, pp. 165-177.

[47] Westerweel, J., Dabiri, D., and Gharib, M., 1997, "Fundamentals of digital particle image velocimetry," Measurement Science and Technology, Vol. 8, pp. 1379-1392.

[48] Willert, E. C., and Gharib, M., 1991, "Digital particle image velocimetry," Experiments in Fluids, Vol. 10, pp. 181-193.